nature structural & molecular biology

Article

https://doi.org/10.1038/s41594-024-01481-6

The structure and function of the ghrelin receptor coding for drug actions

Received: 30 October 2023

Accepted: 20 December 2024

Yuki Shiimura[1,2,9,10] ✉, Dohyun Im[2,9], Ryosuke Tany[3,9], Hidetsugu Asada[2], Ryoji Kise[3], Eon Kurumiya[3], Hideko Wakasugi-Masuho[3], Satoshi Yasuda[4,5], Kazuma Matsui[1], Jun-ichi Kishikawa[6,8], Takayuki Kato[6], Takeshi Murata[4,5], Masayasu Kojima[1], So Iwata[2,10] ✉ & Ikuo Masuho[3,7,10] ✉

Drugs targeting the ghrelin receptor hold therapeutic potential in anorexia, obesity and diabetes. However, developing effective drugs is challenging. To tackle this common issue across a broad drug target, this study aims to understand how anamorelin, the only approved drug targeting the ghrelin receptor, operates compared to other synthetic drugs. Our research elucidated the receptor's structure with anamorelin and miniG$_q$, unveiling anamorelin's superagonistic activity. We demonstrated that ligands with distinct chemical structures uniquely bind to the receptor, resulting in diverse conformations and biasing signal transduction. Moreover, our study showcased the utility of structural information in effectively identifying natural genetic variations altering drug action and causing severe functional deficiencies, offering a basis for selecting the right medication on the basis of the individual's genomic sequence. Thus, by building on structural analysis, this study enhances the foundational framework for selecting therapeutic agents targeting the ghrelin receptor, by effectively leveraging signaling bias and genetic variations.

Ghrelin, a peptide hormone discovered in the stomach, is the endogenous ligand[1] for the ghrelin receptor (GHSR1a), encoded by the *GHSR* gene[2]. It regulates diverse physiological processes, including growth hormone secretion[1], increasing food intake[3], enhancing gastrointestinal motility[4], thermoregulatory effects[5] and many others[6]. The biological importance of ghrelin is underscored by ghrelin receptor mutations causing short stature[7,8], with a severe case linked to compound mutations[9].

The ghrelin receptor belongs to the G-protein-coupled receptor (GPCR) superfamily, comprising over 800 human genes[10]. These receptors translate extracellular stimuli, such as neurotransmitters and hormones, into intracellular signal transduction through heterotrimeric G proteins consisting of Gα, Gβ and Gγ subunits[11]. These proteins fall into four subfamilies ($G_{i/o}$, $G_{q/11}$, G_s and $G_{12/13}$; when α is omitted, it refers to heterotrimeric G proteins in this paper)[12], each driving distinct signaling pathways[13] crucial for drug efficacy. Despite GPCRs being major drug targets—accounting for ~30% of US Food and Drug Administration (FDA)-approved drugs[14]—drug effects on G-protein selectivity remain poorly understood.

Ghrelin receptor-targeted drugs hold therapeutic potential for eating disorders[15], obesity and diabetes[16]. Anamorelin, the first

---

[1]Division of Molecular Genetics, Institute of Life Science, Kurume University, Fukuoka, Japan. [2]Department of Cell Biology, Graduate School of Medicine, Kyoto University, Kyoto, Japan. [3]Pediatrics and Rare Diseases Group, Sanford Research, Sioux Falls, SD, USA. [4]Department of Chemistry, Graduate School of Science, Chiba University, Chiba, Japan. [5]Membrane Protein Research Center, Chiba University, Chiba, Japan. [6]Institute for Protein Research, Osaka University, Osaka, Japan. [7]Department of Pediatrics, Sanford School of Medicine, University of South Dakota, Sioux Falls, SD, USA. [8]Present address: Faculty of Applied Biology, Kyoto Institute of Technology, Kyoto, Japan. [9]These authors contributed equally: Yuki Shiimura, Dohyun Im, Ryosuke Tany. [10]These authors jointly supervised this work: Yuki Shiimura, So Iwata, Ikuo Masuho. ✉e-mail: shiimura_yuuki@kurume-u.ac.jp; s.iwata@mfour.med.kyoto-u.ac.jp; Ikuo.Masuho@SanfordHealth.org

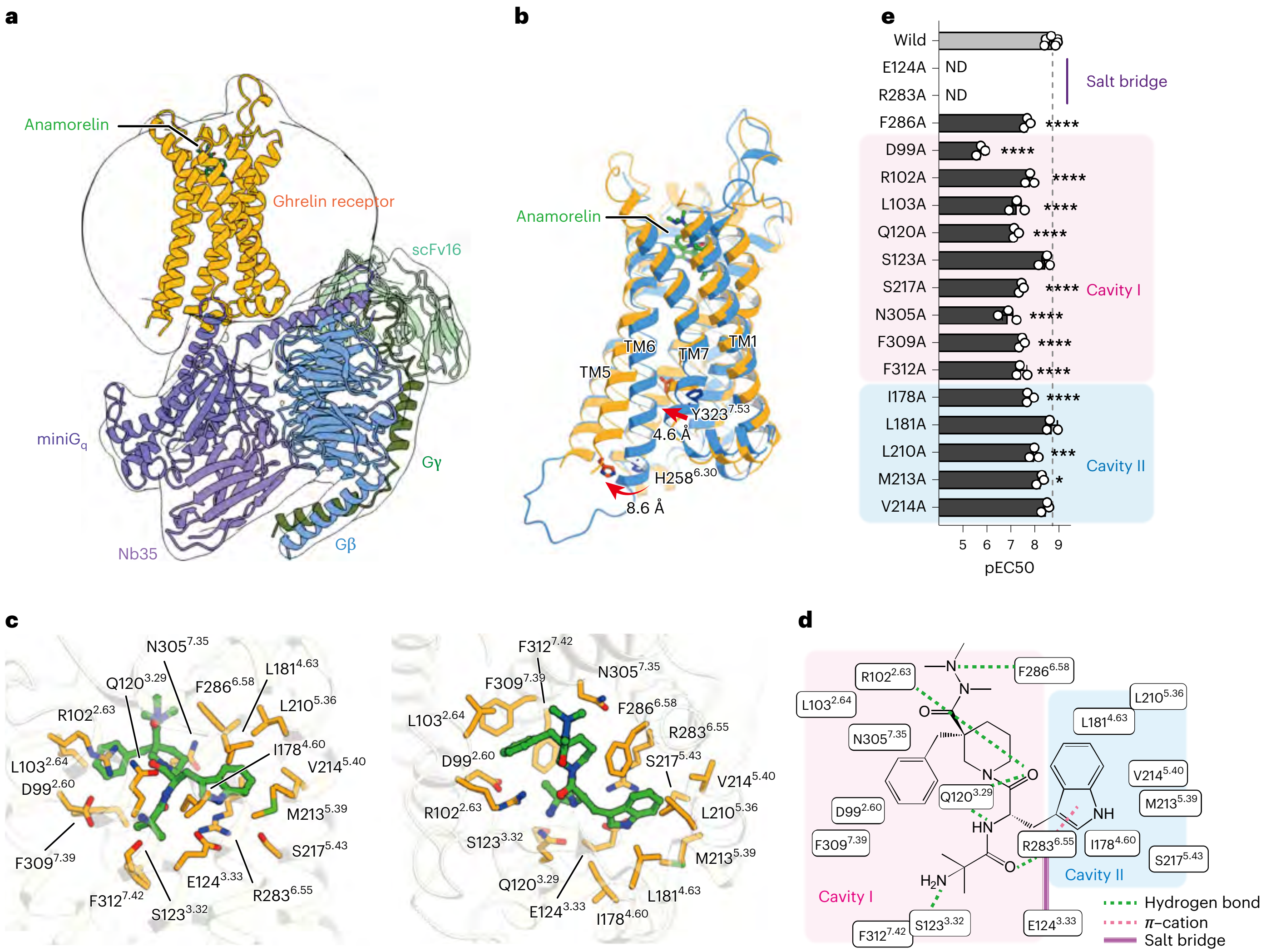

(Side view) (Top view)

Fig. 1 | The structure of anamorelin-bound ghrelin receptor. a, The overall structure of the ghrelin receptor–miniG$_q$ protein complex with bound anamorelin. **b**, Structural superposition of the anamorelin-bound ghrelin receptor (orange; PDB 8JSR) and CPD21-bound ghrelin receptor (blue; PDB 6KO5). **c**, Amino acid residues located within a 4-Å radius of the anamorelin-binding site, emphasizing key interaction points. **d**, A schematic representation of the anamorelin-binding mechanism to the ghrelin receptor, detailing interactions as analyzed using BIOVIA Discovery Studio 2016. **e**, The functional impact of mutant receptors on Ca^{2+} mobilization in response to anamorelin. Data are shown as the mean ± s.e.m. from three independent experiments, each performed in technical quadruplicate. Statistical significance was determined by a one-way analysis of variance (ANOVA) followed by a Dunnett multiple-comparison test, with significance indicated by asterisks ($^{*}P < 0.05$, $^{***}P < 0.001$ and $^{****}P < 0.0001$). Adjusted *P* values in comparison to the wild-type receptor are as follows: <0.0001 for E124A, R283A, F286A, D99A, R102A, L103A, Q120A, S217A, N305A, F309A, F312A and I178A; 0.0001 for L210A; 0.0328 for M213A; 0.5240 for S123A; >0.9999 for L181A; 0.6920 for V214A. ND, not detected.

approved ghrelin receptor agonist, treats cancer cachexia but is currently approved only in Japan for limited cancer types. However, like many therapeutic agents, anamorelin's efficacy varies among receipients[17], underscoring the need for deeper pharmacological and molecular research.

This study revealed the structure of the anamorelin-bound ghrelin receptor with miniG$_q$, showing anamorelin as a superagonist. We made four key findings. Firstly, the receptor's intrinsic guanine nucleotide exchange factor (GEF) activity drives time-dependent and dose-dependent control of G-protein selectivity. Secondly, different ligands induce unique receptor conformations. Thirdly, ligand-induced structural variations in the receptor affect G-protein coupling profiles. Lastly, integration of structural information with genomic and exome sequencing data from 807,162 individuals identified genetic variations that can give rise to rare or ultrarare diseases and influence drug responses. These findings establish a solid foundation for evidence-based treatments tailored to individuals.

Results

The overall structure of anamorelin-bound GHSR1a

Given the importance of anamorelin as the only approved drug targeting the ghrelin receptor, we were motivated to elucidate the ghrelin receptor structure in complex with the drug. Using cryo-electron microscopy (cryo-EM) single-particle analysis, we revealed a ternary complex involving anamorelin, the ghrelin receptor and miniG$_q$ (Fig. 1a and Table 1) at a global resolution of 2.89 Å (Extended Data Fig. 1). This structure closely resembled previously determined active ghrelin receptor structures, bound to ghrelin (Protein Data Bank (PDB) 7F9Y), ibutamoren (PDB 7NA8) and growth hormone-releasing peptide 6 (GHRP6; PDB 7F9Z), with root-mean-square deviation (r.m.s.d.) values of 0.71, 0.83 and 0.94 Å, respectively.

Compared to the antagonist (compound 21 (CPD21))-bound (PDB 6KO5) and the inverse agonist (PF-05190457)-bound (PDB 7F83) inactive ghrelin receptor, the anamorelin-bound structure exhibited notable differences, with r.m.s.d. values of 1.132 and 1.160 Å, respectively. Upon closer examination of the disparities between the anamorelin-bound and antagonist-bound forms, we observed an outward shift of 8.6 Å in transmembrane (TM) 6 (measured at Cα of H258$^{6.30}$) and an inward shift of 4.6 Å in TM7 (measured at Cα of Y323$^{7.35}$) (Fig. 1b), indicating that the anamorelin-bound ghrelin receptor represents the fully active conformation.

Anamorelin-induced unique conformational changes in GHSR1a

GPCR activation by agonist binding leads to G-protein activation through allosteric processes that occur from the extracellular to the intracellular part of GPCR. To understand the effect of anamorelin's effect on this process, we analyzed the anamorelin-bound ghrelin receptor structure in detail (Extended Data Fig. 2), comparing it to structures bound to ghrelin or CPD21. We focused on key motifs involved in the allosteric process, including salt bridges, aromatic clusters, PI(V)F, NPxxY and D(E)RY. The positions and orientations of amino acid residues in the anamorelin-bound structure were more similar to those in the ghrelin-bound structure than in the CPD21-bound structure, aligning with other active ghrelin receptor structures[18–20]. However, the anamorelin-bound structure showed unique differences in certain residues (for example, F312$^{7.42}$ and P224$^{5.50}$) compared to the ghrelin-bound structure (Extended Data Figs. 2 and 3c), suggesting structural changes associated with anamorelin's unique function.

Structural basis of anamorelin binding to GHSR1a

The electron density map allowed precise localization of anamorelin and its interacting amino acid residues (Fig. 1c and Extended Data Fig. 3b). Anamorelin occupied an orthosteric ligand-binding pocket made up of all seven TM helices and extracellular loops (Fig. 1a). This pocket included a large cavity I and a smaller cavity II, separated by a salt bridge formed between E124$^{3.33}$ and R283$^{6.55}$ (Fig. 1d). Anamorelin's major substituents were coordinated within cavity I, while the indole group occupied cavity II.

Closer examination (Fig. 1d) revealed that R283$^{6.55}$, which has a crucial role in forming the salt bridge, establishes a hydrogen bond with anamorelin's central oxygen in cavity I and a π–cation interaction with its indole ring in cavity II. Additionally, R102$^{2.63}$, Q120$^{3.29}$, S123$^{3.32}$ and F286$^{6.58}$ formed hydrogen bonds with anamorelin in cavity I, highlighting the functional importance of cavity I. A pocket formed by eleven additional residues provided further structural support for anamorelin.

Verification of the cryo-EM structure using MD simulations

Advances in computational methods have revolutionized the analysis of structural data, offering powerful tools to investigate molecular interactions at an atomic level. To elucidate the critical binding mechanism of anamorelin, we applied molecular dynamics (MD) simulations as a complementary approach to cryo-EM, addressing the latter's inability to capture structural flexibility.

In two of four 100-ns MD simulations, the binding mode closely aligned with the structure observed in our cryo-EM analysis, providing additional support for its accuracy. However, in the remaining two simulations, the benzene ring of anamorelin penetrated deeper into the ligand-binding pocket, suggesting an alternative binding mode. This alternative conformation highlights the dynamic nature of the ligand–receptor interaction (Supplementary Video 1 and Supplementary Table 1).

Together, these computational approaches provide robust support for the validity of our cryo-EM model while also unveiling additional insights into the structural dynamics of anamorelin binding.

Functional validation of anamorelin–GHSR1a interactions

The binding mechanism of anamorelin with the ghrelin receptor was further validated experimentally by generating alanine mutants of the identified amino acid residues (Fig. 1e and Extended Data Fig. 4). We evaluated the impact of these amino acid substitutions on G$_q$-dependent signaling by assessing intracellular calcium concentration upon ghrelin receptor stimulation with anamorelin.

Most tested mutants negatively affected the half-maximal effective concentration (EC$_{50}$), indicating impaired receptor function. However, three mutants (S123$^{3.32}$A, L181$^{4.63}$A and V214$^{5.40}$A) showed no significant impact on receptor functions. In contrast, functional analysis of natural genetic variations (S123$^{3.32}$G and V214$^{5.40}$L) confirmed the importance of these residues (explained below; Extended Data Fig. 7e).

Table 1 | Cryo-EM data collection, refinement and validation statistics

	Anamorelin–GHSR–miniG$_q$ complex(EMD-36627),(PDB 8JSR)
Data collection and processing	
Magnification	81,000
Voltage (kV)	300
Electron exposure (e– per Å^2)	60, 65^a
Defocus range (μm)	−0.8 to −1.8
Pixel size (Å)	0.88
Symmetry imposed	C_1
Initial particle images (no.)	5,440,034
Final particle images (no.)	1,279,284
Map resolution (Å)	2.89
FSC threshold	0.143
Refinement	
Initial model used (PDB code)	7F9Y
Model resolution (Å)	3.0
FSC threshold	0.5
Map sharpening *B* factor (Å^2)	−27.04
Model composition	
Nonhydrogen atoms	10,074
Protein residues	1,280
Ligands	UYI; 1
B factors (Å^2)	
Protein	55.52
Ligand	100.37
R.m.s.d.	
Bond lengths (Å)	0.004
Bond angles (°)	0.581
Validation	
MolProbity score	1.50
Clashscore	5.80
Poor rotamers (%)	0.46
Ramachandran plot	
Favored (%)	96.91
Allowed (%)	3.09
Disallowed (%)	0

[a] The two merged datasets were each taken with a different electron exposure.

Notably, substitutions of E124$^{3.33}$ and R283$^{6.55}$, crucial for forming the salt bridge, led to a complete loss of function (Fig. 1e and Extended Data Fig. 4a) with negligible impact on expression levels on the plasma

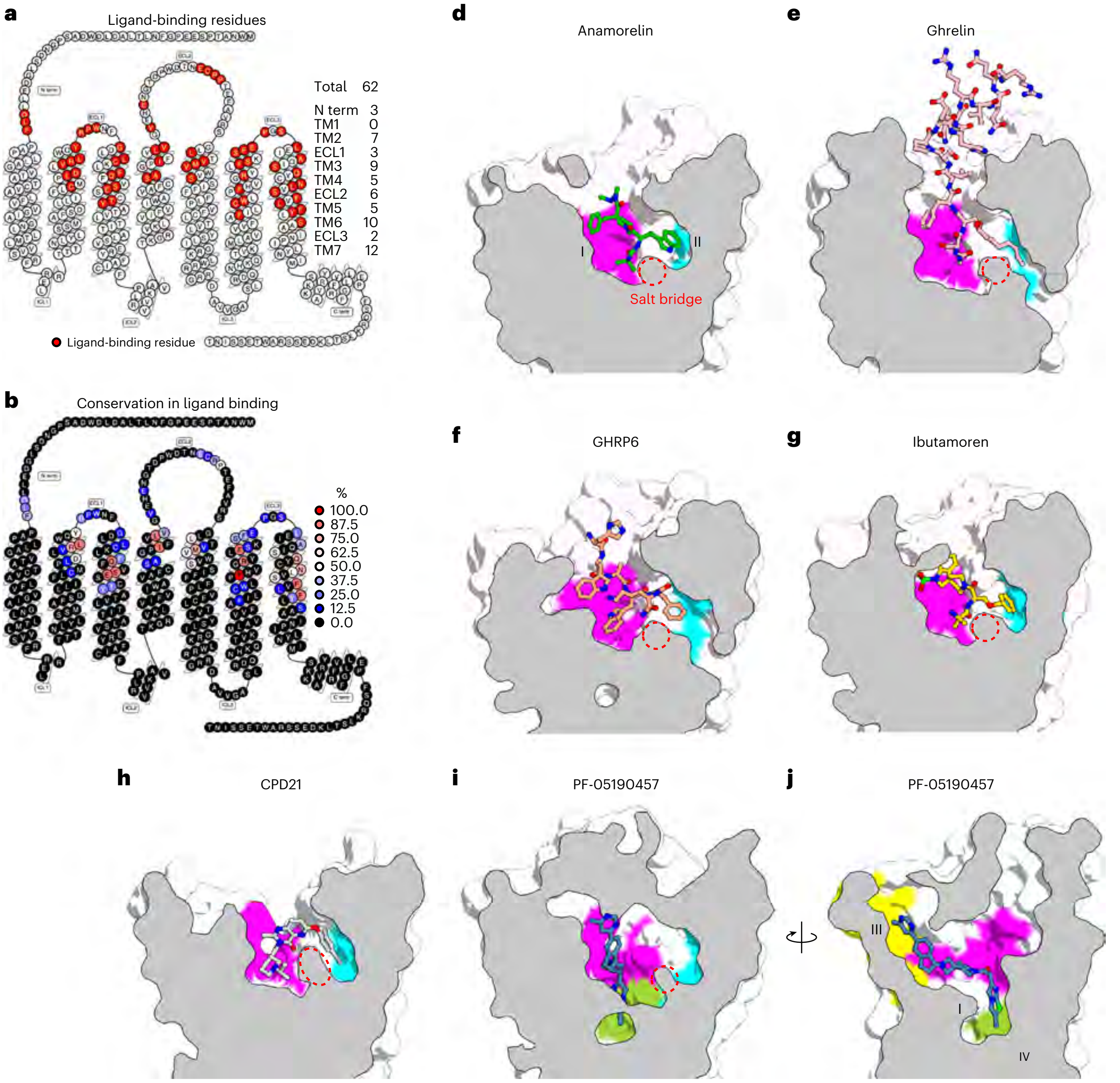

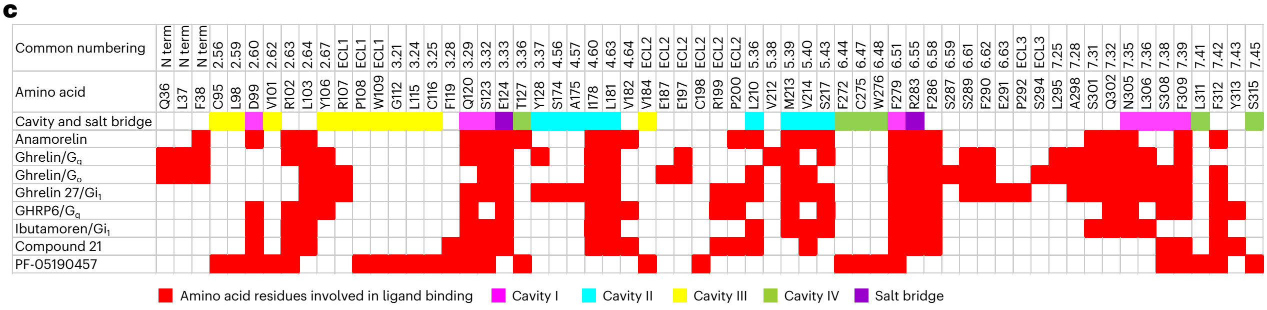

Common numbering	N term	N term	N term	2.56	2.59	2.60	2.62	2.63	2.64	2.67	ECL1	ECL1	ECL1	3.21	3.24	3.25	3.28	3.29	3.32	3.33	3.36	3.37	4.56	4.57	4.60	4.63	4.64
Amino acid	Q36	L37	F38	C95	L98	D99	V101	R102	L103	Y106	R107	P108	W109	G112	L115	C116	F119	Q120	S123	E124	T127	Y128	S174	A175	I178	L181	V182
Cavity and salt bridge				🟨	🟨	🟣	🟨			🟨	🟨	🟨	🟨	🟨	🟨	🟨		🟣	🟣	🟪	🟩	🟦	🟦	🟦	🟦	🟦	
Anamorelin			🟥			🟥		🟥	🟥									🟥	🟥	🟥	🟥				🟥	🟥	🟥
Ghrelin/G$_q$	🟥	🟥	🟥					🟥	🟥	🟥								🟥	🟥	🟥		🟥			🟥	🟥	
Ghrelin/G$_o$	🟥	🟥	🟥						🟥	🟥	🟥								🟥	🟥					🟥	🟥	
Ghrelin 27/Gi$_1$									🟥	🟥	🟥							🟥	🟥	🟥		🟥	🟥	🟥	🟥	🟥	
GHRP6/G$_q$						🟥		🟥	🟥	🟥								🟥		🟥					🟥	🟥	🟥
Ibutamoren/Gi$_1$						🟥		🟥	🟥									🟥	🟥	🟥					🟥	🟥	
Compound 21						🟥		🟥	🟥								🟥	🟥	🟥	🟥					🟥	🟥	🟥
PF-05190457				🟥	🟥	🟥	🟥	🟥				🟥	🟥	🟥	🟥	🟥	🟥	🟥	🟥		🟥						

Common numbering	ECL2	ECL2	ECL2	ECL2	ECL2	ECL2	5.36	5.38	5.39	5.40	5.43	6.44	6.47	6.48	6.51	6.55	6.58	6.59	6.61	6.62	6.63	ECL3	ECL3	7.25	7.28	7.31	7.32	7.35	7.36	7.38	7.39	7.41	7.42	7.43	7.45
Amino acid	V184	E187	E197	C198	R199	P200	L210	V212	M213	V214	S217	F272	C275	W276	F279	R283	F286	S287	S289	F290	E291	P292	S294	L295	A298	S301	Q302	N305	L306	S308	F309	L311	F312	Y313	S315
Cavity and salt bridge	🟨						🟦		🟦	🟦	🟦	🟩	🟩	🟩	🟣	🟪												🟣	🟣	🟣	🟣	🟩			🟩
Anamorelin						🟥	🟥		🟥	🟥	🟥				🟥	🟥	🟥									🟥	🟥	🟥			🟥		🟥		
Ghrelin/G$_q$			🟥					🟥	🟥		🟥				🟥	🟥	🟥		🟥	🟥				🟥	🟥	🟥	🟥	🟥	🟥		🟥				
Ghrelin/G$_o$		🟥	🟥				🟥		🟥	🟥					🟥	🟥	🟥	🟥	🟥	🟥			🟥	🟥	🟥	🟥	🟥	🟥	🟥	🟥	🟥		🟥		
Ghrelin 27/Gi$_1$					🟥	🟥	🟥		🟥	🟥	🟥				🟥	🟥	🟥		🟥	🟥	🟥	🟥			🟥	🟥	🟥	🟥	🟥	🟥	🟥		🟥		
GHRP6/G$_q$					🟥	🟥			🟥		🟥				🟥	🟥	🟥										🟥	🟥		🟥	🟥		🟥	🟥	
Ibutamoren/Gi$_1$							🟥		🟥	🟥	🟥				🟥	🟥	🟥									🟥	🟥	🟥	🟥				🟥		
Compound 21					🟥	🟥	🟥			🟥					🟥	🟥	🟥													🟥	🟥		🟥	🟥	
PF-05190457	🟥			🟥								🟥	🟥	🟥	🟥															🟥	🟥	🟥	🟥		🟥

🟥 Amino acid residues involved in ligand binding 🟣 Cavity I 🟦 Cavity II 🟨 Cavity III 🟩 Cavity IV 🟪 Salt bridge

Fig. 2 | Comparative analysis of ligand binding at the ghrelin receptor. **a**, Visualization of the amino acid residues within the orthosteric ligand-binding pocket of the ghrelin receptor (Supplementary Fig. 1 and Supplementary Table 2). **b**, Quantitative assessment of the importance of each amino acid residue in ligand binding, depicted as the percentage conservation across all analyzed ligands. Amino acids interacting with all ligands are denoted at 100% conservation. **c**, Barcode representation of ligand-binding residues. Amino acids that interact with the ligands, identified from the structures of the ligand-bound ghrelin receptors, are marked in red. **d**–**i**, Cutaway surface views of the ghrelin receptor bound with various ligands. These representations maintain a consistent section of the receptor across all panels, visualizing the receptor from the same viewpoint to enable direct structural comparisons and ensure clarity in observing structural variations. **j**, Binding mode of PF-05190457. For a deeper understanding of PF-05190457's interaction with the receptor, the ligand-binding pocket is illustrated from a unique angle, distinct from that shown in **i**. Cavities within the receptor are color-coded in **d**–**j** for clarity: cavity I, magenta; cavity II, cyan; cavity III, yellow; cavity IV, green. The presence of critical salt bridges is indicated with a red dashed circle in **d**–**j**. The depicted structures were obtained from the PDB under accession codes 8JSR (**d**), 7F9Y (**e**), 7F9Z (**f**), 7NA8 (**g**), 6KO5 (**h**) and 7F83 (**i**,**j**).

membrane (Extended Data Fig. 4b), highlighting the essential role of the salt bridge in shaping the ligand-binding pocket and its critical function in ligand binding rather than affecting the receptor's overall structure.

These functional and computational analyses strongly support the validity of our structural findings.

Overview of ligand-binding mechanisms on GHSR1a

While a single GPCR structure offers valuable insight into ligand–receptor interactions, analyzing multiple receptor structures with diverse ligands enhances our understanding of the receptor structure and ligand recognition. In addition to the anamorelin-bound ghrelin receptor revealed in this study, other ligand-bound and G-protein-bound ghrelin receptor structures have been reported[18–21].

These structural data help understand the mechanism by which drugs act on the ghrelin receptor. We initially mapped all the amino acids involved in ligand binding (Supplementary Fig. 1a–h), uncovering that 62 amino acids contribute to ligand binding (Fig. 2a). Nearly all extracellular structures are involved in ligand binding, while TM1 does not participate.

We further identified specific amino acid residues involved in the interaction with agonists or antagonists and inverse agonists, as well as those binding regardless of drug properties (Supplementary Fig. 1i–k). Agonist-specific binding animo acids are predominantly in TM4–TM7 (Supplementary Fig. 1i), while those specific to antagonists and inverse agonists are in TM2–TM3 and TM6–TM7 (Supplementary Fig. 1j). Common interaction amino acids are distributed across TM2–TM7 (Supplementary Fig. 1k).

Moreover, we determined the conservation of amino acids involved in ligand binding (Fig. 2b) and F279$^{6.51}$ as a key residue binding all ligands, highlighting its critical role. A natural genetic variation at F279$^{6.51}$ significantly diminishes the receptor's activity (Extended Data Figs. 7 and 8).

Overall, these structural analyses provide compelling evidence that distinct ligands interact with specific amino acid residues (Fig. 2c and Supplementary Table 2), implying that each ligand induces unique conformational changes in the ghrelin receptor.

Ligand-induced changes in the orthosteric binding pocket

We next investigated whether variations in the amino acids involved in ligand binding are reflected in the receptor's structure. Using the structural information obtained, we compared the binding modes between anamorelin and other ligands. Cross-sectional analysis of the ligand-binding pocket revealed a flexible pocket with modest changes in size and shape depending on the bound ligand (Fig. 2d–i).

Notably, all ligands exhibited distinct binding modes, reshaping the ligand-binding pocket and supporting the induced-fit model. In particular, the inverse agonist PF-05190457 induced unique structural changes, binding to cavities III and IV (Fig. 2j), which were unoccupied by other ligands. These observations highlight the dynamic nature of ligand–receptor interactions and the potential for diverse receptor conformations in response to different ligands.

Different ligands induce distinct GHSR1a conformations

GPCRs undergo drastic structural rearrangements upon ligand binding within their extracellular pocket to transduce extracellular stimuli into intracellular signal (Fig. 3a). Examining structures in both active and inactive states (Fig. 3b), we observed notable conformational differences at ligand-binding and G-protein-binding sites, indicating specific allosteric modulations based on the bound ligands.

To gain a comprehensive understanding, we systematically compared all available ghrelin receptor structures, dividing them into two regions: the upper half (ligand binding) and the lower half (signal transduction). This allowed us to examine the specific structural changes in these functional regions.

To minimize the impact of varying cryo-EM resolution, we assessed structural similarities among reported ghrelin receptor structures by comparing shifts in the main chain of the TMs (Fig. 3c). In line with the established conformational changes in the TMs during GPCR activation, our analysis revealed that both the lower and the upper regions of the receptor structures exhibited differences when comparing the ghrelin-bound form to those bound with CPD21 or PF-05190457.

While differing in extent, the agonist-bound conformations of anamorelin, ibutamoren and GHRP6 showed distinct characteristics from the ghrelin-bound form in both the extracellular and the intracellular regions. These differences are evident in cross-sections of structures bound to different ligands (Supplementary Fig. 2).

These ligand-induced conformational variabilities may contribute to the functional diversity and distinct signaling outcomes mediated by the ghrelin receptor.

Choice of a functional assay reflecting GPCR structure

To investigate whether the structural differences imply functional differences, we leveraged the bioluminescence resonance energy transfer (BRET) assay, which monitors the activity of nearly all Gα subunits in real time[22,23] (Fig. 4a). A major advantage of the BRET assay is its ability to quantify the G-protein activation rate, reflecting the GEF activity of GPCRs[24]. This unique feature led us to term it as the 'in cellulo GEF assay'.

TS: Please change 'sec' to 's' here.According to well-established principles, enzymes (GPCRs) catalyze faster reactions with their preferred substrates (G proteins). Thus, the rate of G-protein activation provides valuable insights into the selectivity of GPCRs toward G proteins. The strength of GEF activity and, consequently, G-protein selectivity is intrinsically linked to the structural conformation of GPCRs induced by ligand binding[22]. Using this principle, we analyzed the activity associated with structural changes induced by ligand binding.

Intrinsic biochemical properties of GHSR1a

Using the BRET assay, we first determined the G-protein selectivity of the ghrelin receptor upon stimulation with a saturated concentration of ghrelin (Supplementary Fig. 3a–c). This experiment was performed with a panel of G proteins, excluding transducin and gustducin, which are predominantly expressed in specialized cell types (Fig. 4b). Our results showed that the ghrelin receptor activates G proteins in the $G_{i/o}$, $G_{q/11}$ and $G_{12/13}$ subfamilies, with no notable activation of the G_s subfamily (Fig. 4c,d and Extended Data Fig. 5a,b).

Quantitative measurement of GEF activity revealed that the ghrelin receptor is a promiscuous G_qPCR (Fig. 4e and Extended Data Fig. 5c). The G-protein coupling pattern changes over time because of differences in GEF activity for each G protein (Fig. 4f–h). Additionally, different G proteins are activated depending on ghrelin concentration (Fig. 4i). These observations characterize the biochemical properties and a G-protein coupling profile for the ghrelin-bound receptor (Fig. 4d,e), serving as a benchmark for evaluating the properties of other ligands on the receptor.

Anamorelin functions as a superagonist on GHSR1a

We next investigated the characteristics of the ghrelin receptor bound to anamorelin, comparing its activity to that of the receptor bound to ghrelin (Fig. 5a–c). This experiment involved four representative G proteins from three G-protein subfamilies, G_{oA}, G_q and G_{13} (from the $G_{i/o}$, $G_{q/11}$ and $G_{12/13}$ subfamilies, respectively), as well as G_{15}, an atypical G protein known for its promiscuous coupling with broad GPCRs[25] and its exceptionally slow deactivation rate[26]. G proteins belonging to the G_s subfamily were excluded as they showed no coupling with the ghrelin-bound receptor (Fig. 4).

Comparing the activation patterns of G proteins by ghrelin and anamorelin, we observed that, while the agonist-induced maximum amplitude remained consistent for G_q, it increased for the other three

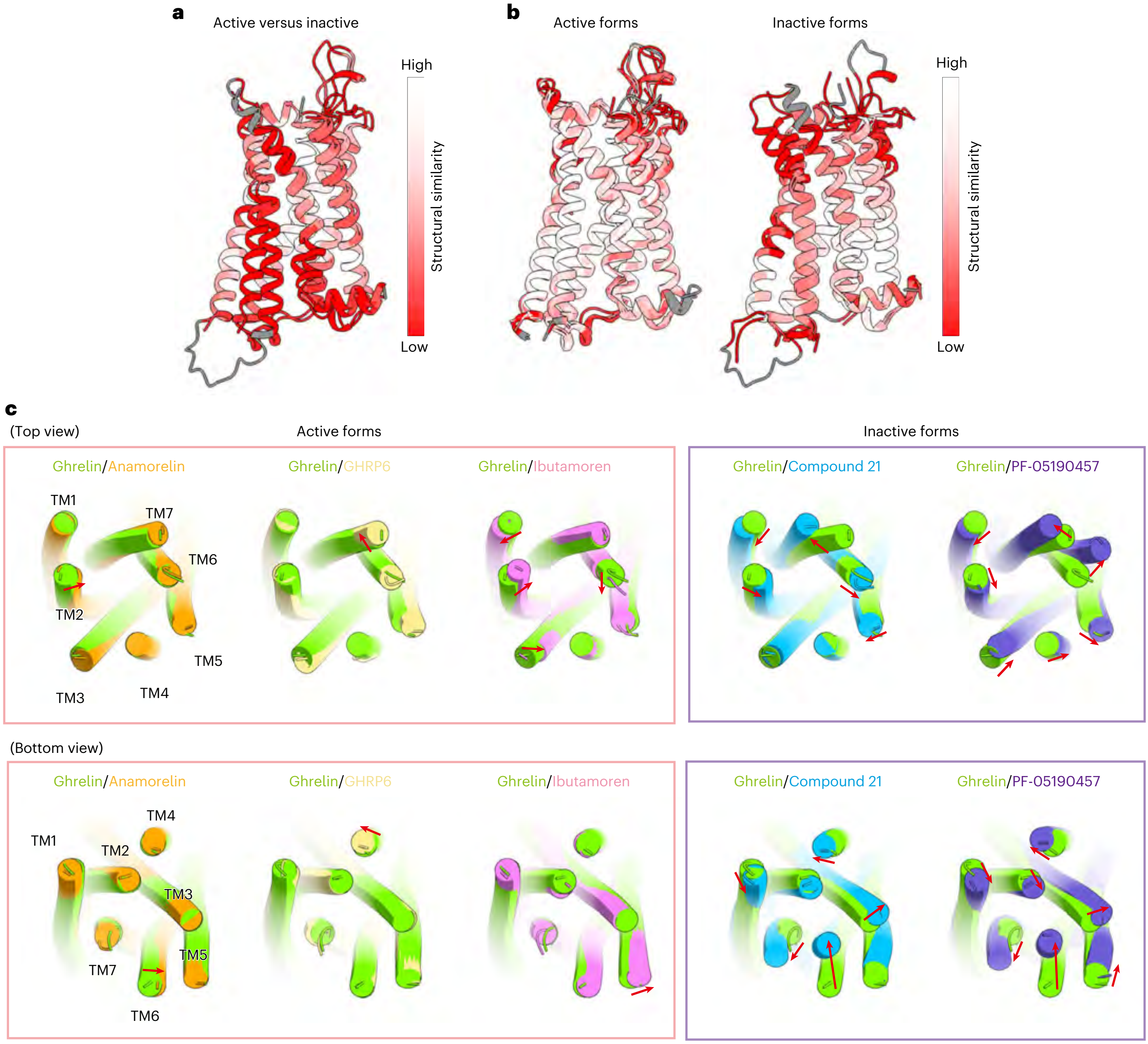

Fig. 3 | Comparative analyses of ligand-bound ghrelin receptor structures. **a**, Structural comparison between the ghrelin receptor bound to anamorelin (PDB 8JSR) and CPD21 (PDB 6KO5). **b**, Analysis of the overall structures within active states (PDB 7F9Y versus 8JSR, 7F9Z or 7NA8) and within inactive states (PDB 6KO5 versus 7F83). Unaligned residues are depicted gray in **a**,**b**. **c**, Detailed comparison of the upper (ligand-binding) and lower (G-protein-binding) regions of the ghrelin receptor structure across different ligand complexes. The depicted structures were obtained from the PDB under accession codes 7F9Y, 8JSR, 7F9Z, 7NA8, 6KO5 and 7F83. The red arrows indicate structural shifts greater than 1.7 Å in the Cα of the amino acid at the ends of the TM regions.

G proteins (Fig. 5a,b). The activation rates of all examined G proteins were enhanced (Fig. 5a,c), indicating that anamorelin acts as a superagonist. Notably, ghrelin and anamorelin each induce unique patterns of G-protein activation, with significant variations in both the degree and the speed of activation across different G proteins (Fig. 5b,c).

Additionally, ibutamoren also acts as a superagonist (Extended Data Fig. 6a–c) but with a distinct balance of effects on G-protein activation rate compared to anamorelin (Extended Data Fig. 6c versus Fig. 5c). These results suggest that the ghrelin-bound, anamorelin-bound and ibutamoren-bound receptors adopt different conformations, influencing signaling properties. Thus, our elucidation of the ghrelin receptor structure bound to anamorelin greatly enriches the limited collection of GPCR structures associated with superagonists[27].

Ligand properties shape GHSR1a signaling bias

This study identified superagonists using GEF activity as a measurement in living cells. Motivated by these findings, we investigated additional ligands using our BRET-based approach to quantitatively examine ligand properties on the ghrelin receptor (Fig. 5d–i).

To delve deeper into this investigation, we examined the partial agonist AwFw-LL[28] (Fig. 5d–f). While the full agonist ghrelin activated G_q, G_{oA}, G_{15} and G_{13}, AwFw-LL selectively activated G_q and showed no activity on G_{15}. Even at a lower concentration, where the ghrelin-induced G_q activation rate was slower than that of AwFw-LL, ghrelin stimulation clearly activated G_{oA}, G_{15} and G_{13} (Extended Data Fig. 6d–f), highlighting structural differences between the ghrelin receptor conformations induced by ghrelin and AwFw-LL binding.

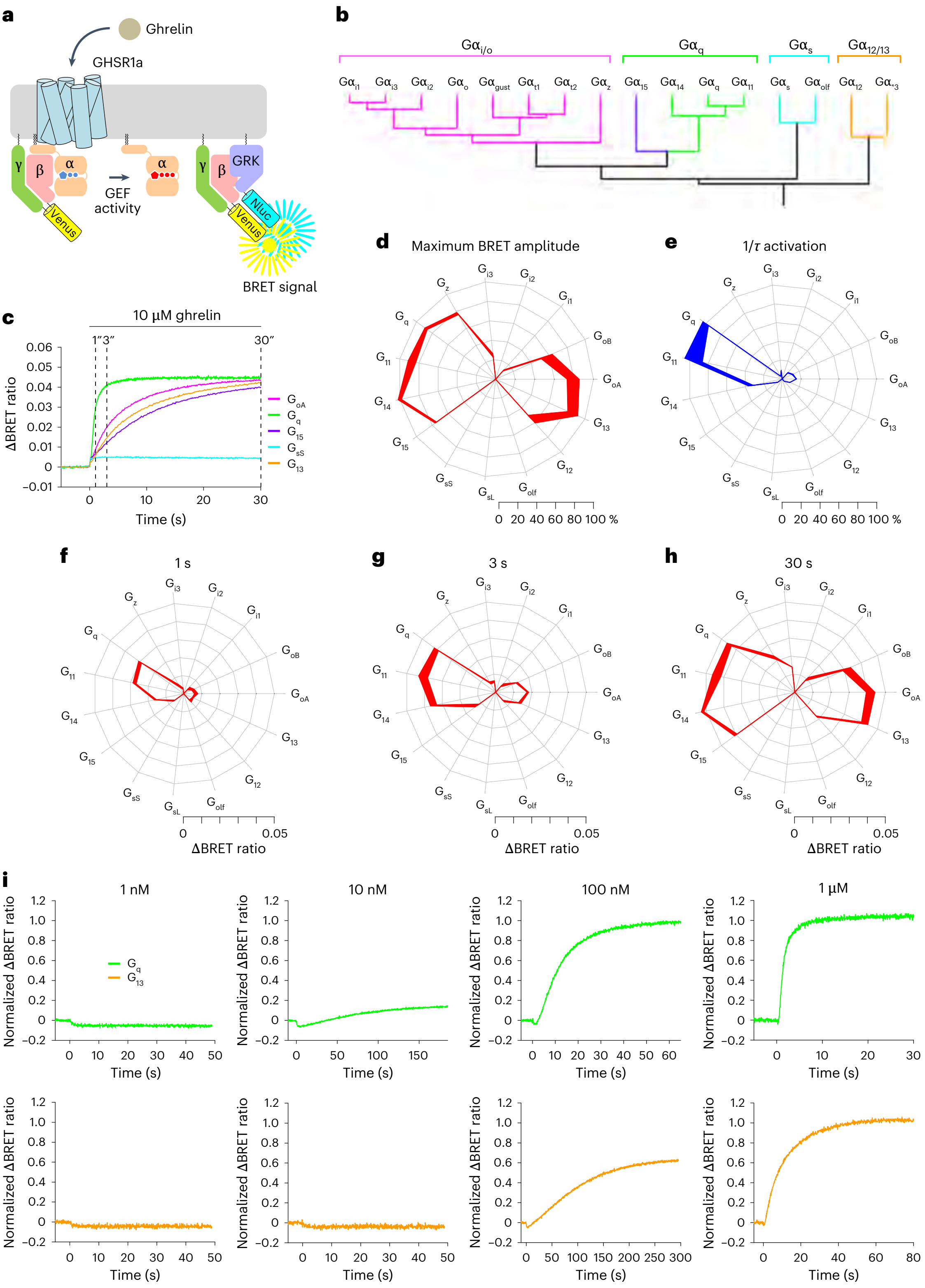

Fig. 4 | Biochemical characteristics of the ghrelin-activated ghrelin receptor. **a**, Diagram of the BRET-based kinetic assay used for real-time monitoring of receptor activity triggered by ghrelin. Activation of the ghrelin receptor by an agonist leads to the dissociation of inactive heterotrimeric G proteins into active guanosine triphosphate (GTP)-bound Gα and Venus–G$\beta_1\gamma_2$ dimer. The free Venus–Gβγ, dissociated from GTP-bound Gα, interacts with the Gβγ effector mimetic masGRK3ct–Nluc–HA, producing a BRET signal. **b**, Phylogenetic tree of human Gα subunits, constructed with MEGA-X (https://www.megasoftware.net/). **c**–**e**, Quantitative analysis of the G-protein selectivity profile of the ghrelin receptor induced by ghrelin. HEK293T/17 cells, transfected with the ghrelin receptor and a BRET sensor pair along with distinct Gα subunits, were treated with a saturated ghrelin dose of 10 μM (Supplementary Fig. 3a–c) at time zero, followed by monitoring changes in the BRET signal (**c**). Radar plots illustrate the maximum response amplitude (**d**) and activation kinetics (**e**) across different G proteins. Line thickness in the radar plots represents the s.e.m. in **d**,**e**. τ is the time constant derived from the kinetics of the observed response. **f**–**h**, Temporal G-protein coupling profiles of the ghrelin receptor at 1 s (**f**), 3 s (**g**) and 30 s (**h**) after stimulation. **i**, Response to different concentrations of ghrelin. The traces represent the mean values of three independent experiments in **c**,**i**. Data are shown as the mean ± s.e.m. of three independent experiments in **d**–**h**.

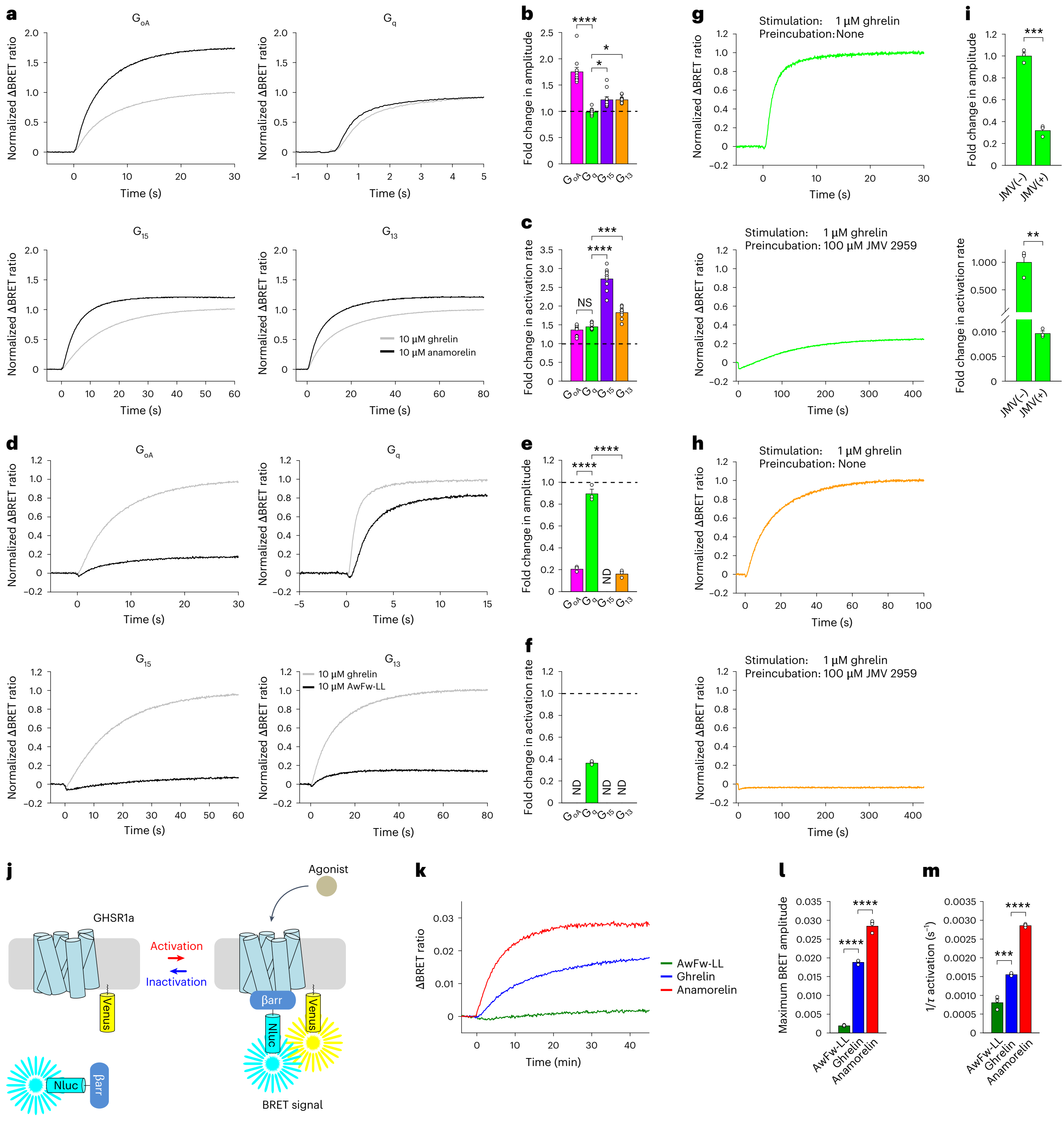

Fig. 5 | Quantitative analysis of ligand properties on the ghrelin receptor. **a**–**i**, Quantitative assessment of ghrelin receptor activity in response to anamorelin (**a**–**c**), AwFw-LL (**d**–**f**) and JMV 2959 (**g**–**i**) using an in cellulo GEF assay. Saturated concentrations of ghrelin, anamorelin and AwFw-LL were determined in Supplementary Fig. 3. **a**,**d**, Normalized BRET responses to the maximum amplitude induced by 10 μM ghrelin are shown. **g**,**h**, Normalized BRET responses to 1 μM ghrelin without preincubation with JMV 2959 are shown. **j**, Diagram of β-arrestin recruitment assay. **k**–**m**, Quantitative characterization of the ghrelin receptor in response to AwFw-LL (10 μM), ghrelin (10 μM) and anamorelin (10 μM) using a β-arrestin recruitment assay. The traces represent the mean values of ten independent experiments (**a**) or three independent experiments (**d**,**g**,**h**,**k**). Data are shown as the mean ± s.e.m. of ten independent experiments (**b**,**c**) or three independent experiments (**e**,**f**,**i**,**l**,**m**) in bar graphs. Statistical significance was determined by a one-way ANOVA with a Dunnett multiple-comparison test (**b**,**c**,**e**,**l**,**m**) and unpaired two-tailed *t*-test (**i**), with significance indicated by asterisks ($*P < 0.05$, $**P < 0.01$, $***P < 0.001$ and $****P < 0.0001$). Adjusted *P* values are as follows: <0.0001 for G$_q$ versus G$_{oA}$, 0.0157 for G$_q$ versus G$_{15}$ and 0.0163 for G$_q$ versus G$_{13}$ (**b**); 0.8959 for G$_q$ versus G$_{oA}$, <0.0001 for G$_q$ versus G$_{15}$ and 0.0003 for G$_q$ versus G$_{13}$ (**c**); <0.0001 for G$_q$ versus G$_{oA}$ and G$_q$ versus G$_{13}$ (**e**); 0.0001 for amplitude and 0.0022 for activation rate (**i**); <0.0001 for ghrelin versus AwFw-LL and ghrelin versus anamorelin (**l**); 0.0002 for ghrelin versus AwFw-LL and <0.0001 for ghrelin versus anamorelin (**m**). The activation rates were not determined for G$_{oA}$ and G$_{13}$ in **f** because of small responses that could not be accurately quantified for activation rates. NS, not statistically significant ($P > 0.05$).

Results with anamorelin and AwFw-LL indicate that agonists can bias G-protein coupling. We further explored whether antagonists could bias signaling. Of the ligands tested (JMV 2959, YIL 781, CPD21 and PF-05190457), only JMV 2959 showed neutral antagonist activity (Supplementary Fig. 4), leading to its selection for the subsequent experiments. Pretreatment with JMV 2959 inhibited ghrelin-induced G_{13} activation while leaving G_q activation (Fig. 5g–i), demonstrating that antagonists can bias G-protein coupling.

Our findings reveal the complexities of drug action on the ghrelin receptor. Structural (Figs. 2 and 3) and functional (Figs. 4 and 5) observations indicate that the unique interaction mechanisms between ligands and the receptor influence the receptor's GEF activity and G-protein selectivity. These results emphasize the importance of considering the strength of GEF activity and G-protein selectivity in GPCR-targeted therapy.

Arrestin recruitment in drug action

To explore the drug's mechanism of action further, we examined the initial step of arrestin-mediated desensitization: arresting mobilization to the plasma membrane (Fig. 5j). Without transfecting G proteins to observe natural responses from endogenous G proteins, we found that AwFw-LL, primarily inducing G_q activity (Fig. 5d–f), hardly recruited arrestin to the plasma membrane (Fig. 5k–m). However, agonists with stronger GEF activity and promiscuous G-protein coupling (Fig. 5a–c) intensified and accelerated arrestin recruitment (Fig. 5k–m).

Genetic diversity of *GHSR*

Current treatments often fail to account for genetic variability, influencing drug response[29]. Advances in sequencing technologies have revealed numerous single-nucleotide polymorphism (SNPs)[30] and disease-related genes[31], yet applying this knowledge to essential GPCR targets such as the ghrelin receptor remains challenging.

Using data from gnomAD version 4.0 (https://gnomad.broadinstitute.org/), we analyzed natural genetic variations in the ghrelin receptor across over 807,000 individuals[32]. Missense variations (MVs) were distributed throughout the receptor, affecting 84% of amino acid residues (Fig. 6a and Supplementary Table 3).

On the basis of the probabilistic analysis, approximately 99.4% of people do not possess any MV within this receptor (Fig. 6b). All identified MVs are rare, with allele frequencies ranging from 0.01% to less than 1%, or ultrarare, with frequencies less than 0.01% (Fig. 6c). No common variant with more than 1% allele frequency was observed, highlighting the receptor's essential physiological role.

Because rare and ultrarare variants are more likely to have deleterious effects[33,34], investigating their functional importance is crucial.

Variations in ligand-binding pocket impact ghrelin actions

To apply sequence information in therapeutics effectively, it is essential to identify both disease-causing variants[35] and those that alter drug action among benign SNPs[36]. Leveraging structural information is a powerful approach to identifying mutations that impact drug action[36] and contribute to disease development[26].

We, therefore, conducted a functional analysis on mutations impacting residues within the ligand-binding pocket, commonly implicated in ligand interactions (Figs. 2b and 6a). Additionally, we included the A204$^{\mathrm{ECL2}}$E mutant, associated with short stature because of low basal activity[7], as a representative pathogenic variant.

First, we examined the response of these mutants to ghrelin compared to the wild-type receptor (Fig. 6d and Extended Data Fig. 7), assessing amplitude, activation rates and basal activity. All mutants exhibited abnormalities in at least one parameter (Extended Data Fig. 7), demonstrating the efficiency of our approach in identifying mutants with functional deficiencies. Notably, the N305$^{7.35}$K mutant showed a complete loss of function (Fig. 6d), more severe than the pathogenic A204$^{\mathrm{ECL2}}$E mutant (Extended Data Fig. 7b).

Distinct responsiveness of the N305$^{7.35}$K mutant to ligands

Given the notable functional abnormality of the N305$^{7.35}$K substitution, we examined whether its functionality could be restored by various agonists (GHRP6, anamorelin and ibutamoren) (Fig. 6e–g).

The N305$^{7.35}$K mutant showed distinct responses to different agonists (Fig. 6d–g). It was unresponsive to the peptide ligand GHRP6 (Fig. 6e) but was activated to varying degrees by the small-molecule drugs ibutamoren and anamorelin (Fig. 6f,g). Preincubation with ghrelin or GHRP6 did not inhibit the response to anamorelin, indicating a loss of binding ability to these peptide ligands (Fig. 6h,i).

We also investigated the response of N305$^{7.35}$K to antagonists and an inverse agonist (Extended Data Figs. 8 and 9). N305$^{7.35}$K affected the inhibitory effect of JMV 2959 and PF-05190457 (Extended Data Fig. 9c,e) but had no significant impact on YIL 781 and CPD21 activity (Extended Data Fig. 9g,i).

Taken together, results with eight different ligands demonstrate that each MV within the ligand-binding pocket uniquely influences drug efficacy (Fig. 6 and Extended Data Figs. 7–9), consistent with our structural analysis of ligand-binding mechanisms (Fig. 2 and Supplementary Fig. 1).

Structural basis of drug actions on the N305$^{7.35}$K variant

Leveraging the ligand-bound ghrelin receptor's structures, we analyzed how N305$^{7.35}$K impacts drug actions. Our analysis revealed that N305$^{7.35}$ is responsible for binding to all four agonists examined but their binding modes are different (Fig. 6j). Specifically, this residue forms a crucial hydrogen bond with ghrelin and GHRP6 and its substitution with lysine disrupts this bond, likely causing the complete loss of binding ability (Fig. 6d,e,h).

In contrast, both anamorelin and ibutamoren rely less on this residue. Anamorelin's benzyl group usesN305$^{7.35}$ and the lysine substitution may maintain or enhance binding, explaining the limited impact on ibutamoren's and anamorelin's activity (Fig. 6f,g).

For antagonists and the inverse agonist, there is no reported structure for the JMV 2959-bound and YIL 781-bound receptor. Therefore, we analyzed the structures of CPD21-bound and PF-05190457-bound receptors, finding N305$^{7.35}$ to be 5.78 and 4.64 Å away, respectively (Extended Data Fig. 9k). This suggests N305$^{7.35}$'s involvement in PF-05190457 binding but not CPD21 binding, explaining our functional analysis results (Extended Data Fig. 9e,i).

Thus, our functional and structural analyses strongly suggest that N305$^{7.35}$ has a crucial role in determining drug actions targeting the ghrelin receptor.

Discussion

This study presents the structure of the ghrelin receptor bound by anamorelin, the only approved drug targeting this receptor in clinics, bringing the total number of reported ghrelin receptor structures to eight. Comparing these structures shows that ligands with different chemical structures bind uniquely, resulting in diverse receptor structures and functions. This highlights that chemical design can modify drug selectivity, affinity, downstream signaling pathways, cellular response and efficacy, potentially reducing adverse side effects.

Additionally, our research demonstrates that measuring the GEF activity of GPCRs in living cells can precisely elucidate ligand nature, uncovering mechanisms of action that reflect ligand-bound GPCR structures. Moreover, by analyzing genomic and exome sequences from 807,162 individuals alongside structural information, we can efficiently identify natural genetic variations that may be pathogenic or affect drug action mechanisms. These insights lay the groundwork for data-driven, evidence-based treatment.

Roles of structural biology and GEF assay in drug design

As structural analyses of GPCRs progress rapidly, drug discoveries targeting GPCRs are transiting from random to rational approaches[37].

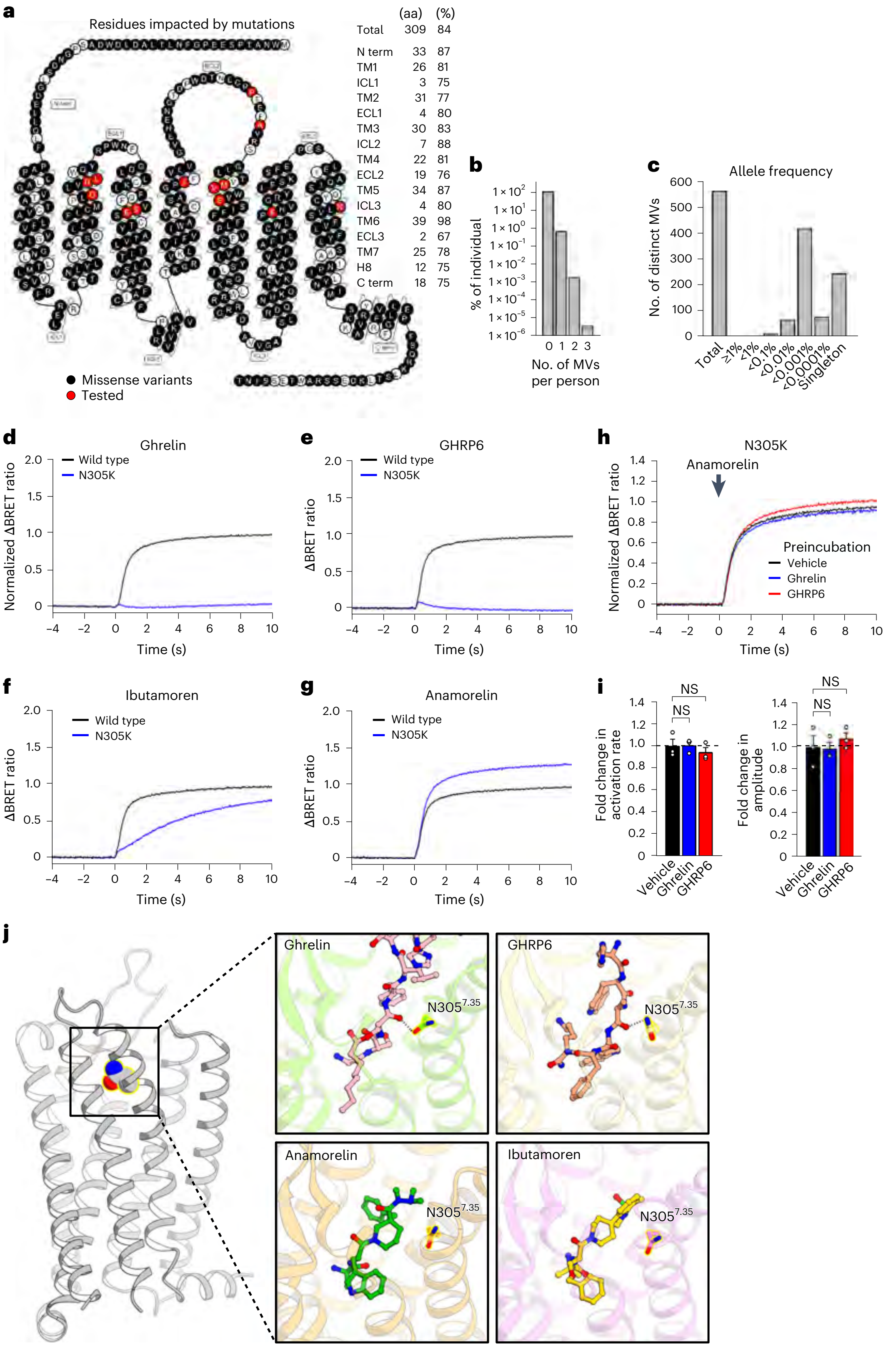

Fig. 6 | Impact of N305$^{7.35}$K substitution on drug actions. a, Residues in the ghrelin receptor impacted by mutations. The positions of MVs tested in this study are highlighted in red. **b**, Probability of individuals with MVs in the ghrelin receptor. **c**, Number of unique MVs in the ghrelin receptor per frequency. **d**–**g**, Impact of N305$^{7.35}$K on the action of agonists. Four agonists were used: ghrelin (**d**), GHRP6 (**e**), ibutamoren (**f**) and anamorelin (**g**). The saturated concentration (10 μM) of agonist was applied to cells (Supplementary Fig. 3). **h**,**i**, Examination of possible antagonistic activity of ghrelin and GHRP6 on N305$^{7.35}$K. Transfected cells were preincubated with 10 μM ghrelin or 10 μM GHRP6 for 1 min and then stimulated with 10 μM anamorelin. **j**, Binding modes of N305$^{7.35}$ and ligands. Hydrogen bonds are shown as dotted lines. The traces represent the mean values of four independent experiments (**g**) or three independent experiments (**d**–**f**,**h**). Data are shown as the mean ± s.e.m. of three independent experiments in **i**. Statistical significance was determined using a one-way ANOVA with a Dunnett multiple-comparison test. NS, not statistically significant ($P > 0.05$).

The number of GPCR structures has now reached several hundred[38], enabling in silico drug design[39] and screening[40]. For instance, successful drug screening targeting the dopamine D4 receptor has been reported[41].

After discovering a ligand and elucidating the structure of the ligand-bound receptor, demonstrating how the drug acts on GPCR is crucial for determining the therapeutic value. Despite progress in structural analysis, no functional assay quantitatively reflects GPCR structure, hampering rational drug design. As a unique approach, we used a method to measure GEF activity that intrinsically reflects the structure of ligand-bound GPCRs in a living cell environment.

In this study, we quantitatively illustrated the G-protein selectivity induced by ghrelin as an intrinsic biochemical property of the ghrelin receptor (Fig. 4). This G-protein selectivity profile was compared to that induced by chemically synthesized ligands (Fig. 5), allowing us to investigate ligand nature quantitatively. For example, we revealed that anamorelin is a superagonist with a unique conformation, highlighting the importance of strong GEF activity for treating cancer cachexia. This study sets the stage for advancements in GPCR-targeted therapies, as discussed further below.

The dynamic nature of GHSR1a-induced signaling

Understanding of GPCR signal transduction has evolved to reveal its intricate and complex nature[42]. Particularly noteworthy is the fact that many GPCRs can couple with multiple types of G proteins[22,43,44]. This study demonstrated that the ghrelin receptor functions as a G_qPCR, displaying promiscuity by also coupling with G proteins from the $G_{i/o}$ and $G_{12/13}$ subfamilies (Fig. 4d,e). This G-protein coupling pattern changes dynamically over time (Fig. 4f–h) and is influenced by agonist concentration (Fig. 4i). Such inherent complexity in all GPCRs[22,45] provides a wide range of functional possibilities, explaining their role in diverse physiological phenomena and evolutionary success[46]. However, drug discovery has yet to fully exploit this unique characteristic.

Signaling bias driven by ligand properties

The precise role of promiscuous G-protein coupling in GPCRs remains unclear. However, for the ghrelin receptor, G_q signaling regulates food intake[47], while G_{i2} influences insulin release[48]. As such, controlling G-protein selectivity at the ghrelin receptor may lead to more effective therapy.

Our findings show that ligands induce distinct receptor conformations, leading to varying GEF activity across different G proteins (Fig. 5 and Extended Data Fig. 6a–c). Even antagonists and an inverse agonist were capable of signaling bias (Fig. 5g–i and Supplementary Fig. 4), suggesting that combining ligands, such as an agonist and an antagonist, could fine-tune signaling outcomes.

These results demonstrate the potential of our in cellulo GEF assay for quantitatively classifying drugs on the basis of their G-protein coupling profiles, providing a framework for selecting ligands tailored to enhance therapeutic efficacy and minimize side effects.

Toward treatment based on individual genetic differences

A rational treatment approach must consider genetic variations[36,49] in addition to controlling G-protein selectivity.

Using structural and genomic information, our study identified mutants (for example, R102$^{2.63}$P, S217$^{5.43}$P and F279$^{6.51}$L) causing more dramatic functional abnormalities than the pathogenic A204^{ECL2}E mutant[7] (Extended Data Fig. 7b,f), potentially indicating the pathogenicity of these mutants or their roles in nondisease characteristics[50].

Notably, the N305$^{7.35}$K mutant, unable to bind to the endogenous agonist ghrelin, resulted in a complete loss of function (Fig. 6d,h,i). This mutant also failed to bind the peptide agonist GHRP6 but responded to small chemical compounds anamorelin and ibutamoren (Fig. 6e–i and Extended Data Fig. 7c–e). Thus, conditions resulting from N305$^{7.35}$K can be treated with anamorelin or ibutamoren, depending on the need.

We also showed that mutations can alter antagonist and inverse agonist activity (Extended Data Fig. 8). Many mutations transformed antagonists into agonists. For inverse agonists, mutations weakened their activity but did not alter their function as agonists (Extended Data Fig. 8e). This suggests inverse agonists are a safer choice for suppressing ghrelin receptor activity, with less impact from mutations.

While it is crucial to acknowledge that human genomes are diploid, these results emphasize the need to account for natural genetic variations before using drugs. This approach moves from a one-treatment-fits-all model to tailored treatment for individuals[29].

Conclusion

In summary, we demonstrated that effective ghrelin receptor-targeted therapy can be achieved by understanding the receptor's intrinsic biochemical properties (Fig. 4) and structure (Figs. 1–3), the ligand-induced signaling bias (Fig. 5) and the impact of mutations on drug actions (Fig. 6). This ensures that appropriate therapeutic agents can be administered to the appropriate persons. Most importantly, this enticing concept is applicable to a broad range of drug targets. Considering that approximately 30% of FDA-approved drugs target GPCRs, the impact of genetic variations on drug actions on GPCRs is a substantial economic burden[36]. Therefore, our strategy for efficient identification of genetic variants that alter drug action is crucial for establishing pharmacogenetics targeting GPCRs.

Online content

Any methods, additional references, Nature Portfolio reporting summaries, source data, extended data, supplementary information, acknowledgements, peer review information; details of author contributions and competing interests; and statements of data and code availability are available at https://doi.org/10.1038/s41594-024-01481-6.

References

1. Kojima, M. et al. Ghrelin is a growth-hormone-releasing acylated peptide from stomach. *Nature* **402**, 656–660 (1999).
2. Howard, A. D. et al. A receptor in pituitary and hypothalamus that functions in growth hormone release. *Science* **273**, 974–977 (1996).
3. Nakazato, M. et al. A role for ghrelin in the central regulation of feeding. *Nature* **409**, 194–198 (2001).
4. Masuda, Y. et al. Ghrelin stimulates gastric acid secretion and motility in rats. *Biochem. Biophys. Res. Commun.* **276**, 905–908 (2000).
5. Szentirmai, E., Kapas, L., Sun, Y., Smith, R. G. & Krueger, J. M. The preproghrelin gene is required for the normal integration of thermoregulation and sleep in mice. *Proc. Natl Acad. Sci. USA* **106**, 14069–14074 (2009).
6. Collden, G., Tschop, M. H. & Muller, T. D. Therapeutic potential of targeting the ghrelin pathway. *Int. J. Mol. Sci.* **18**, 798 (2017).
7. Pantel, J. et al. Loss of constitutive activity of the growth hormone secretagogue receptor in familial short stature. *J. Clin. Invest.* **116**, 760–768 (2006).
8. Inoue, H. et al. Identification and functional analysis of novel human growth hormone secretagogue receptor (*GHSR*) gene mutations in Japanese subjects with short stature. *J. Clin. Endocrinol. Metab.* **96**, E373–E378 (2011).
9. Pantel, J. et al. Recessive isolated growth hormone deficiency and mutations in the ghrelin receptor. *J. Clin. Endocrinol. Metab.* **94**, 4334–4341 (2009).
10. Fredriksson, R., Lagerstrom, M. C., Lundin, L. G. & Schioth, H. B. The G-protein-coupled receptors in the human genome form five main families. Phylogenetic analysis, paralogon groups, and fingerprints. *Mol. Pharmacol.* **63**, 1256–1272 (2003).
11. Offermanns, S. G-proteins as transducers in transmembrane signalling. *Prog. Biophys. Mol. Biol.* **83**, 101–130 (2003).

12. Downes, G. B. & Gautam, N. The G protein subunit gene families. *Genomics* **62**, 544–552 (1999).
13. Wettschureck, N. & Offermanns, S. Mammalian G proteins and their cell type specific functions. *Physiol. Rev.* **85**, 1159–1204 (2005).
14. Hauser, A. S., Attwood, M. M., Rask-Andersen, M., Schioth, H. B. & Gloriam, D. E. Trends in GPCR drug discovery: new agents, targets and indications. *Nat. Rev. Drug Discov.* **16**, 829–842 (2017).
15. Fazeli, P. K. et al. Treatment with a ghrelin agonist in outpatient women with anorexia nervosa: a randomized clinical trial. *J. Clin. Psychiatry* **79**, 17m11585 (2018).
16. Wiedmer, P., Nogueiras, R., Broglio, F., D'Alessio, D. & Tschop, M. H. Ghrelin, obesity and diabetes. *Nat. Clin. Pract. Endocrinol. Metab.* **3**, 705–712 (2007).
17. Temel, J. S. et al. Anamorelin in patients with non-small-cell lung cancer and cachexia (ROMANA 1 and ROMANA 2): results from two randomised, double-blind, phase 3 trials. *Lancet Oncol.* **17**, 519–531 (2016).
18. Wang, Y. et al. Molecular recognition of an acyl-peptide hormone and activation of ghrelin receptor. *Nat. Commun.* **12**, 5064 (2021).
19. Qin, J. et al. Molecular mechanism of agonism and inverse agonism in ghrelin receptor. *Nat. Commun.* **13**, 300 (2022).
20. Liu, H. et al. Structural basis of human ghrelin receptor signaling by ghrelin and the synthetic agonist ibutamoren. *Nat. Commun.* **12**, 6410 (2021).
21. Shiimura, Y. et al. Structure of an antagonist-bound ghrelin receptor reveals possible ghrelin recognition mode. *Nat. Commun.* **11**, 4160 (2020).
22. Masuho, I. et al. Distinct profiles of functional discrimination among G proteins determine the actions of G protein-coupled receptors. *Sci. Signal.* **8**, ra123 (2015).
23. Masuho, I., Skamangas, N. K. & Martemyanov, K. A. Live cell optical assay for precise characterization of receptors coupling to $G\alpha_{12}$. *Basic Clin. Pharmacol. Toxicol.* **126**, 88–95 (2020).
24. Masuho, I., Xie, K. & Martemyanov, K. A. Macromolecular composition dictates receptor and G protein selectivity of regulator of G protein signaling (RGS) 7 and 9—2 protein complexes in living cells. *J. Biol. Chem.* **288**, 25129–25142 (2013).
25. Offermanns, S. & Simon, M. I. $G\alpha_{15}$ and $G\alpha_{16}$ couple a wide variety of receptors to phospholipase C. *J. Biol. Chem.* **270**, 15175–15180 (1995).
26. Masuho, I. et al. A global map of G protein signaling regulation by RGS proteins. *Cell* **183**, 503–521 (2020).
27. Maeda, S., Qu, Q., Robertson, M. J., Skiniotis, G. & Kobilka, B. K. Structures of the M1 and M2 muscarinic acetylcholine receptor/G-protein complexes. *Science* **364**, 552–557 (2019).
28. Holst, B. et al. Identification of an efficacy switch region in the ghrelin receptor responsible for interchange between agonism and inverse agonism. *J. Biol. Chem.* **282**, 15799–15811 (2007).
29. Roden, D. M. & George, A. L.Jr The genetic basis of variability in drug responses. *Nat. Rev. Drug Discov.* **1**, 37–44 (2002).
30. Goodwin, S., McPherson, J. D. & McCombie, W. R. Coming of age: ten years of next-generation sequencing technologies. *Nat. Rev. Genet.* **17**, 333–351 (2016).
31. Rabbani, B., Tekin, M. & Mahdieh, N. The promise of whole-exome sequencing in medical genetics. *J. Hum. Genet.* **59**, 5–15 (2014).
32. Karczewski, K. J. et al. The mutational constraint spectrum quantified from variation in 141,456 humans. *Nature* **581**, 434–443 (2020).
33. Kryukov, G. V., Pennacchio, L. A. & Sunyaev, S. R. Most rare missense alleles are deleterious in humans: implications for complex disease and association studies. *Am. J. Hum. Genet.* **80**, 727–739 (2007).
34. Subramanian, S. Quantifying harmful mutations in human populations. *Eur. J. Hum. Genet.* **20**, 1320–1322 (2012).
35. Ashley, E. A. Towards precision medicine. *Nat. Rev. Genet.* **17**, 507–522 (2016).
36. Hauser, A. S. et al. Pharmacogenomics of GPCR drug targets. *Cell* **172**, 41–54 (2018).
37. Congreve, M., de Graaf, C., Swain, N. A. & Tate, C. G. Impact of GPCR structures on drug discovery. *Cell* **181**, 81–91 (2020).
38. Kooistra, A. J. et al. GPCRdb in 2021: integrating GPCR sequence, structure and function. *Nucleic Acids Res.* **49**, D335–D343 (2021).
39. Wang, S. et al. D_4 dopamine receptor high-resolution structures enable the discovery of selective agonists. *Science* **358**, 381–386 (2017).
40. Stein, R. M. et al. Virtual discovery of melatonin receptor ligands to modulate circadian rhythms. *Nature* **579**, 609–614 (2020).
41. Lyu, J. et al. Ultra-large library docking for discovering new chemotypes. *Nature* **566**, 224–229 (2019).
42. Hermans, E. Biochemical and pharmacological control of the multiplicity of coupling at G-protein-coupled receptors. *Pharmacol. Ther.* **99**, 25–44 (2003).
43. Inoue, A. et al. Illuminating G-protein-coupling selectivity of GPCRs. *Cell* **177**, 1933–1947 (2019).
44. Avet, C. et al. Effector membrane translocation biosensors reveal G protein and βarrestin coupling profiles of 100 therapeutically relevant GPCRs. *eLife* **11**, e74101 (2022).
45. Himmelreich, S. et al. Dopamine receptor DAMB signals via G_q to mediate forgetting in *Drosophila*. *Cell Rep.* **21**, 2074–2081 (2017).
46. de Mendoza, A., Sebe-Pedros, A. & Ruiz-Trillo, I. The evolution of the GPCR signaling system in eukaryotes: modularity, conservation, and the transition to metazoan multicellularity. *Genome Biol. Evol.* **6**, 606–619 (2014).
47. Mende, F. et al. Translating biased signaling in the ghrelin receptor system into differential in vivo functions. *Proc. Natl Acad. Sci. USA* **115**, E10255–E10264 (2018).
48. Dezaki, K., Kakei, M. & Yada, T. Ghrelin uses $G\alpha_{i2}$ and activates voltage-dependent K^+ channels to attenuate glucose-induced Ca^{2+} signaling and insulin release in islet β-cells: novel signal transduction of ghrelin. *Diabetes* **56**, 2319–2327 (2007).
49. Schoneberg, T. & Liebscher, I. Mutations in G protein-coupled receptors: mechanisms, pathophysiology and potential therapeutic approaches. *Pharmacol. Rev.* **73**, 89–119 (2021).
50. Lango Allen, H. et al. Hundreds of variants clustered in genomic loci and biological pathways affect human height. *Nature* **467**, 832–838 (2010).

Methods

Complementary DNA (cDNA) constructs

Ghrelin receptor (NM_198407) in pcDNA3.1(+) and its mutants were synthesized by GenScript. Gα_{oA} (NM_020988) in pcDNA3.1(+) was a gift from K. Martemyanov. Gα_{oB} (AH002708), Gα_z (J03260), Gα_{11} (AF493900), Gα_{14} (NM_004297), Gα_{15} (AF493904), Gα_s long isoform (Gα_{sL}) (NM_000516), Gα_{olf} (AF493893), Gα_{12} (NM_007353) and Gα_{13} (NM_006572) in pcDNA3.1(+) were purchased from the cDNA Resource Center (www.cDNA.org). The pCMV5 plasmids encoding rat Gα_{i1}, rat Gα_{i2}, rat Gαi3, human Gα_q and bovine Gα_s short isoform (Gα_{sS}) were kindly provided by H. Itoh. The Venus (156–239)–Gβ_1, Venus (1–155)–Gγ_2 and mVenus–KRas were generously gifted by N. A. Lambert[51]. FLAG-tagged Ric-8A (NM_053194) in pcDNA3.1 was a gift from J.-P. Montmayeur[52]. FLAG-tagged Ric-8B (NM_183172 with a single MV (A1586G)) in pcDNA3.1 was a gift from B. Malnic[53]. mas-GRK3ct–Nluc–HA[22] and pertussis toxin (PTX-S1; AJ920066) were reported previously[54]. β-arrestin 2–Nluc (β-arrestin 2 (NM_004313) fused to a GGSGGG linker at the N terminus of Nluc was a gift from K. Martemyanov.

Mutagenesis of the ghrelin receptor

The full-length human ghrelin receptor was cloned into a pCAGGS expression vector with an HA signal sequence followed by a FLAG epitope tag at the N terminus and an 8×His-tag at the C terminus[21]. Most ghrelin receptor mutants were previously described[21]. To generate mutants that were not previously produced, the KOD One PCR master mix (TOYOBO) was used. These constructs were used in Fig. 1 and Extended Data Fig. 4.

Cloning and expression of GHSR1a complex in *Spodoptera frugiperda* (Sf9) cells

The full-length human ghrelin receptor was cloned into a modified pFastBac1 vector (Invitrogen). The vector contained an expression cassette with an HA signal sequence, a FLAG epitope tag and an 8×His-tag. These were followed by a thermostabilized apocytochrome b_{562}RIL (bRIL) epitope from *Escherichia coli* (M7W, H102I and R106L) to improve the expression level. A human rhinovirus (HRV) 3C protease cleavage site was inserted between the ghrelin receptor and bRIL. Additionally, a large fragment of NLuc was fused to the receptor's C terminus.

For miniG$_q$, cloned into pFastBac1, a dominant-negative miniG$_s$ skeleton with the Gα_{i1} N terminus was used to enable binding to Nb35 and scFv16. Bovine Gγ_2 and a 10×His-tagged rat Gβ_1 with a C-terminal HiBiT tag were subcloned into the pFastBac Dual vector. Ric-8A, a molecular chaperone, was likewise cloned into pFastBac1 vector.

Recombinant baculoviruses were generated using the Bac-to-Bac baculovirus expression system (Invitrogen). Sf9 insect cells (Thermo Fisher Scientific, B82501) were infected with baculovirus at a cell density of $2–3.5 \times 10^6$ cells per ml in PSFM-J1 medium (Wako) supplemented with 2% (v/v) fetal calf serum, 50 U per ml penicillin, 50 μg ml^{-1} streptomycin and 0.5 μg ml^{-1} amphotericin B. The ghrelin receptor, miniG$_q$, G$\beta_1\gamma_2$ and Ric-8A were coinfected at a multiplicity of infection ratio of 8:2:2:1. Cells were harvested by centrifugation 48 h after infection and the cell pellets were stored at −80 °C for future use.

Expression and purification of Nb35 and scFv16

Nb35 and scFv16 were expressed using the *Brevibacillus* expression system (Takara). *B. choshinensis* cells transformed with Nb35 or scFv16 were kindly provided by N. Nomura. Transformed cells were cultured at 30 °C for 3 days in a medium containing 40 g L^{-1} soytone, 5 g L^{-1} yeast extract, 20 g L^{-1} glucose, 0.15 g L^{-1} CaCl$_2$ and 50 mg L^{-1} neomycin.

Ammonium sulfate was added to the collected culture supernatant to a final concentration of 60% to precipitate the proteins. The precipitate was collected by centrifugation at 11,100*g* for 20 min at 4 °C, dissolved in a TBS buffer (10 mM Tris-HCl pH 7.5 and 150 mM NaCl) and dialyzed overnight in the same buffer.

The dialyzed sample was purified using Ni-NTA resin and treated with 6×His-tagged tobacco etch virus (TEV) protease, followed by overnight dialysis in TBS buffer. Cleaved mCherry–10×His-tagged and 6×His-tagged TEV protease were removed using a HisTrap column (Cytiva). The flowthrough fractions were further purified using a HiLoad 16/600 Superdex 75-pg column (Cytiva) equilibrated with TBS buffer. Peak fractions were pooled, concentrated to 2.5 mg ml^{-1}, flash-frozen in liquid nitrogen and stored at −80 °C.

Complex purification

The cell pellets were resuspended in a buffer containing 20 mM HEPES pH 7.5, 100 mM NaCl, 10% glycerol, 5 mM MgCl$_2$, 5 mM CaCl$_2$, 0.25 mM TCEP, protease inhibitor cocktail (Nacalai Tesque), 25 mU per ml of apyrase and 2 μM anamorelin and stirred for 1 h at room temperature. Cell membranes were isolated by ultracentrifugation at 100,000*g* for 30 min at 4 °C, then solubilized for 2 h at 4 °C in a solubilization buffer containing 20 mM HEPES pH 7.5, 100 mM NaCl, 10% glycerol, 5 mM MgCl$_2$, 5 mM CaCl$_2$, 0.25 mM TCEP, a protease inhibitor cocktail, 25 mU per ml of apyrase, 0.5% (w/v) lauryl maltose neopentyl glycol (LMNG, Anatrace) with 0.05% (w/v) cholesteryl hemisuccinate (CHS, Sigma-Aldrich) and 2 μM anamorelin. Insoluble materials were removed by ultracentrifugation at 100,000*g* for 30 min at 4 °C.

The supernatants were incubated with TALON metal affinity resin (Clontech) for 2 h at 4 °C. The resin was than washed with ten column volumes of wash buffer containing 20 mM HEPES pH 7.5, 100 mM NaCl, 10% glycerol, 2 mM MgCl$_2$, 2 mM CaCl$_2$, 20 mM imidazole, 0.25 mM TCEP, 0.01% (w/v) LMNG, 0.01% (w/v) glyco-diosgenin (GDN; Anatrace), 0.001% (w/v) CHS and 2 μM anamorelin. The complex was eluted with three column volumes of elution buffer containing 20 mM HEPES pH 7.5, 100 mM NaCl, 10% glycerol, 2 mM MgCl$_2$, 2 mM CaCl$_2$, 250 mM imidazole, 0.25 mM TCEP, 0.01% (w/v) LMNG, 0.001% (w/v) GDN (Anatrace), 0.001% (w/v) CHS and 10 μM anamorelin.

TALON elution fractions were mixed with Nb35, scFv16 and HRV 3C protease and stirred overnight at 4 °C to cleave the N-terminal FLAG tag, 8×His-tag and bRIL epitope. The protein complex was concentrated to 0.5 ml using an Amicon Ultra-15 concentrator (Millipore) and then purified by size-exclusion chromatography on a Superdex 200 Increases 10/300 column (GE Healthcare) pre-equilibrated with a buffer containing 20 mM HEPES pH 7.5, 100 mM NaCl, 2 mM MgCl$_2$, 2 mM CaCl$_2$, 0.25 mM TCEP, 0.0015% (w/v) LMNG, 0.0005 (w/v) GDN, 0.00015% (w/v) CHS and 20 μM anamorelin. Monomeric complex fractions were collected, concentrated to ~10 mg ml^{-1} and used for EM experiments.

Cryo-EM grid preparation and data collection

Quantifoil R1.2/1.3 holey carbon copper grid (Quantifoil) was glow-discharged at 7 Pa with 10 mA for 10 s using a JEC-3000FC sputter coater (JEOL) before sample application. A 3-μl aliquot of samples was applied to the grid, blotted for 5 s with a blot force of 10 in 100% humidity at 8 °C and then plunged into liquid ethane using a Vitrobot Mark IV (Thermo Fisher Scientific).

Cryo-EM data collection for screening sample quality and grid conditions was performed on a Glacios cryo-transmission EM instrument operated at 200 kV with a Falcon4 camera (Thermo Fisher Scientific) at the Institute for Life and Medical Sciences, Kyoto University. Following screening, final data collection was conducted on a Titan Krios (Thermo Fisher Scientific) operated at 300 kV equipped with a direct K3 electron detector, Gatan BioQuantum energy filter (20-eV slit width) (Gatan) and Cs corrector (CEOS) at the Institute for Protein Research, Osaka University.

Data collection occurred in two separate sessions using SerialEM software at a nominal magnification of ×81,000 (calibrated pixel size of 0.88 Å per pixel). For the first session, a total exposure time of 5.82 s across 60 frames was used; for the second session, 6.503 s across 65 frames was used. Both sessions used a defocus range of −0.8 to −1.8 μm. Detailed imaging conditions are described in Table 1.

Cryo-EM data processing

Image stacks for both datasets of the anamorelin-bound ghrelin receptor–miniG$_q$ complex were processed using MotionCor2.1 for beam-induced motion correction[55]. Dose-weighted micrographs were imported into cryoSPARC version 3.2 (Structura Biotechnology)[56], where contrast transfer function (CTF) parameters were estimated using the patch CTF estimation tool.

For the first dataset, particles were initially selected using the Blob particle picker. Initial two-dimensional (2D) classification was performed to generate templates for template-based particle picking. A subset of the selected particles was used to train Topaz, which was subsequently used for particle repicking from the micrographs[57]. The picked particles were extracted with a pixel size of 1.1 Å per pixel and subjected to 2D classification to discard poorly defined particles. Ab initio reconstruction was performed in cryoSPARC, generating four classes: one well-defined class and three trash classes. Multiple rounds of heterogeneous refinement were applied to the four ab initio models to remove low-quality particles. The selected particles were then extracted at full pixel size (0.88 Å per pixel) and refined using nonuniform (NU) refinement.

For the second dataset, particles were selected using the template picker with 2D templates derived from the previous NU refinement. The picked particles were extracted at a pixel size of 2.2 Å per pixel and subjected to 2D classification to exclude poorly defined particles. Multiple rounds of heterogeneous refinement were applied using the four ab initio models from first dataset. The selected particles were extracted at full pixel size and further refined with NU refinement.

The datasets were subsequently merged and additional 2D classification and heterogeneous refinement were performed to obtain the final particles. NU refinement was applied to generate the final map, with resolutions estimated using the gold-standard Fourier shell collection (FSC = 0.143) criterion. Local resolution was calculated in cryoSPARC and map sharpening was reevaluated using the PHENIX autosharpen tool. These processed maps were used for modeling. The overall processing strategy is illustrated in Extended Data Fig. 1.

Model building and refinement

Model building was guided by the previously determined cryo-EM structures of the GHSR1a–miniG$_q$ complex (PDB 7F9Z)[18]. The receptor, miniG$_q$ trimer, Nb35 and scFv16 models were manually constructed in Coot[58] and subsequently refined through multiple rounds of real-space refinement using PHENIX[59]. Molecular graphics were generated using CueMol2 (http://www.cuemol.org) and UCSF ChimeraX[60]. The statistics for the three-dimensional reconstruction and model refinement are summarized in Table 1.

Identifying ligand interactions with the ghrelin receptor

To investigate the ligand-binding and Gα-binding mechanisms to the ghrelin receptor, we used LigPlot$^+$ version 2.2.8 (https://www.ebi.ac.uk/thornton-srv/software/LigPlus/). Structural models from the PDB (https://www.rcsb.org/) were first protonated using ChimeraX version 1.7.1 (https://www.cgl.ucsf.edu/chimerax/) and interactions were subsequently analyzed with LigPlot$^+$. The analysis was conducted by adjusting two parameters from the default settings. Specifically, the Maximum D–A distance was set to 4 Å and the maximum contact distance was set to 5 Å to account for protein structure flexibility.

Creation of snake plots

The snake plots were created using GPCRdb (https://gpcrdb.org/).

Visualization of local structural differences

Structural variations in ghrelin receptors bound to different ligands were visualized using color-coded Cα r.m.s.d. maps in ChimeraX (Fig. 3a,b). In this analysis, regions of high structural variance are indicated in red, whereas areas of high homology are shown in white. Residues not included in the superposition are displayed in gray.

Cell surface expression assay

The cell surface expression of wild-type and mutant ghrelin receptors was evaluated using a fluorescence-activated cell sorting (FACS) assay. HEK293 cells (American Type Culture Collection (ATCC), CRL-1573) were seeded in 24-well plates at a density of 3.5×10^5 cells per well and cultured at 37 °C in 5% CO_2 for 24 h. The cells were transfected with FuGENE HD transfection reagent (Promega).

The following day, transfected cells were harvested in PBS containing 1 mM EDTA and incubated on ice for 30 min with 2.5 μg ml^{-1} anti-FLAG antibody (Wako) and 5 μg ml^{-1} Alexa Fluor 488-conjugated anti-mouse IgG goat polyclonal antibody (Thermo Fisher Scientific) in FACS buffer (PBS with 2% FBS and 0.05% NaN_3). After washing with FACS buffer, FLAG-positive cells were analyzed using a Guava EasyCyte Plus flow cytometer (Merck Millipore).

The mean fluorescence intensity (MFI) of each mutant was determined using Cytosoft version 5.3.1 (Merck Millipore). The MFI of the mutant receptors was normalized to that of the wild-type ghrelin receptor, which was measured in parallel, and expressed as relative levels.

Ca^{2+} mobilization assay

A fluorescence-based assay was used to detect changes in intracellular Ca^{2+} concentration ($[Ca^{2+}]_i$). CHO-K1 cells (ATCC, CCL-61) were seeded in 6-cm dishes at a density of 3×10^5 cells per dish and transfected with either wild-type or mutant ghrelin receptor constructs using FuGENE HD transfection reagent. The following day, transfected cells were harvested and plated into 96-well black plates (Corning) at a density of 2.5×10^4 cells per well.

After a 24-h incubation, the cells were loaded with 100 μl of calcium indicator from the FLIPR Calcium 5 assay kit (Molecular Devices) in Hanks' balanced salt solution containing 20 mM HEPES–NaOH pH 7.5 and 3 mM probenecid. The cells were incubated for 1 h at 37 °C before testing. Changes in fluorescence, indicative of calcium mobilization, were measured using a FlexStation3 (Molecular Devices) following the addition of 50 μl of anamorelin at various concentrations.

Maximum $[Ca^{2+}]_i$ changes were determined in quadruplicate and normalized to the response elicited by 1 μM ionomycin. EC_{50} values for each dose–response curve were calculated using GraphPad Prism 9 software.

Transfection for fast kinetic BRET assay

HEK293T/17 cells (ATCC, CRL-11268) were cultured in DMEM supplemented with 10% FBS, nonessential amino acids, 1 mM sodium pyruvate and antibiotics (100 U per ml penicillin and 100 μg ml^{-1} streptomycin) at 37 °C in a 5% CO_2 humidified incubator. Before seeding, 3.5-cm culture dishes were coated with 1 ml of Matrigel solution (approximately 10 μg ml^{-1} growth factor-reduced Matrigel (Corning) in culture medium) at 37 °C for 5 min.

Cells were seeded at a density of 2×10^6 cells per dish and, after 2 h, transfection was performed using 5 μg of expression constructs and 5 μl of 1 mg ml^{-1} PEI Max per dish. The ghrelin receptor (1), Gα (Gα$_{oA}$ (2), Gα$_{oB}$ (1), Gα$_{i1}$ (1), Gα$_{i2}$ (2), Gα$_{i3}$ (1.5), Gα$_z$ (1.5), Gα$_q$ (2), Gα$_{11}$ (2), Gα$_{14}$ (4), Gα$_{15}$ (2), Gα$_s$ short (6), Gα$_s$ long (4), Gα$_{olf}$ (6), Gα$_{12}$ (3) or Gα$_{13}$ (4)), Venus (156–239)–Gβ$_1$ (1), Venus (1–155)–Gγ$_2$ (1) and masGRK3ct–Nluc–HA (1) were transfected (the number in parentheses indicates the ratio of transfected DNA (ratio 1 = 0.21 μg for dish)). Gα$_{14}$, Gα$_{15}$ and Gα$_{olf}$ required coexpression with molecular chaperones Ric-8A or Ric-8B to generate functional G-protein complexes, as previously reported[22]. A catalytic subunit of pertussis toxin (PTX-S1) was coexpressed with Gα$_z$, Gα$_q$, Gα$_{11}$, Gα$_{14}$, Gα$_{15}$, Gα$_s$ (short or long), Gα$_{olf}$, Gα$_{12}$ or Gα$_{13}$ to inhibit possible endogenous G$_{i/o}$ coupling. An empty pcDNA3.1(+) vector was used to normalize total transfected DNA.

Fast kinetic BRET assay (in cellulo GEF assay)

Agonist-induced BRET responses between Venus–Gβγ and masGRK3ct–Nluc–HA sensors were measured as described previously[22,61]. Then, 16–24 h after transfection, cells were washed with BRET buffer

(PBS containing 0.5 mM $MgCl_2$ and 0.1% glucose), detached and resuspended in BRET buffer. Approximately 50,000–100,000 cells per well were distributed in 96-well plates. Furimazine (Promega) was used as the Nluc substrate following the manufacturer's instructions.

BRET measurements were performed at room temperature using a microplate reader (FLUOstar Omega or PHERAstar FSX; BMG Labtech). The BRET signal is determined by calculating the ratio of the light emitted by the Venus–Gβγ over the light emitted by Nluc. The basal BRET ratio before agonist stimulation was subtracted to calculate the ΔBRET ratio, with the largest ΔBRET value representing the maximum BRET amplitude. The activation rate constants ($1/\tau$) were determined by fitting a single exponential curve to the traces using Clampfit 10.3.

From our experience, it has been observed that responses measured by cellular assays can vary greatly with the cellular state. Consequently, when undertaking comparisons between two different conditions—such as comparing various mutants against the wild-type receptor or analyzing responses to distinct ligands—we make it a point to only compare data from experiments conducted on the same day for consistency.

β-arrestin recruitment assay

Similar to the transient transfection described above for HEK293T/17 cells, the cells were transiently transfected with the ghrelin receptor (1), β-arrestin 2–Nluc (0.1) and mVenus–KRas (2) constructs. The numbers in parentheses represent the ratios used for transfection, where a ratio of 1 denotes 0.21 μg for a 3.5-cm dish. The day after transfection, the cells were used in experiments similar to the in cellulo GEF assay. The cells were used to assess the recruitment of β-arrestin 2 to the activated ghrelin receptor, which is indicated by an increase in BRET between the Nluc and the Venus.

MD simulation of the anamorelin-bound ghrelin receptor

We used the cryo-EM structure of the anamorelin-bound ghrelin receptor. The structure was inserted into a model membrane constructed by a 1-palmitoyl-2-oleoyl-*sn*-glycero-3-phosphocholine (POPC) lipid bilayer. It was immersed in the TIP3P water where NaCl (0.10 mol L^{-1}) was dissolved. The membrane builder in the CHARMM-GUI web interface[62,63] was used to perform the insertion and system pre-equilibration. Parameters and molecular topologies for the ligands were generated on the basis of the CGenFF force field[64]. The initial box size was 100 Å × 100 Å × 122 Å. The numbers of POPC lipids, water molecules, sodium ions and chloride ions were 259, 25,941, 46 and 60, respectively. MD simulations were performed with AMBER 20 (https://ambermd.org/), using the CHARMM36m force field. The time step was set at 2.0 fs and the bond lengths with H atoms were constrained using the SHAKE algorithm. Electrostatic interactions were calculated using particle mesh Ewald. We used the nonbonded cutoff at 12 Å and applied the Langevin thermostat and the Monte Carlo barostat to regulate temperature and pressure, respectively. We conducted a 100-ns product simulation in the NPT ensemble at 298.15 K and 1 atm. The force constant for the restraints on the backbone atoms was at 1 kcal per mol per $Å^2$.

Statistical analysis

All of the statistical analyses were performed with GraphPad Prism version 9.

Reporting summary

Further information on research design is available in the Nature Portfolio Reporting Summary linked to this article.

Data availability

The cryo-EM density maps and atomic coordinates were deposited to the EM Data Bank and PDB under accession numbers EMD-36627 and 8JSR for the anamorelin-bound ghrelin receptor–miniG$_q$ complex. The initial coordinates, simulation input files and final output coordinate file from our MD simulations, conducted in four independent replicates, were deposited to the Biological Structure Model Archive under accession code BSM00078. Source data are provided with this paper.

References

51. Hollins, B., Kuravi, S., Digby, G. J. & Lambert, N. A. The C-terminus of GRK3 indicates rapid dissociation of G protein heterotrimers. *Cell Signal.* **21**, 1015–1021 (2009).
52. Fenech, C. et al. Ric-8A, a Gα protein guanine nucleotide exchange factor potentiates taste receptor signaling. *Front. Cell. Neurosci.* **3**, 11 (2009).
53. Von Dannecker, L. E., Mercadante, A. F. & Malnic, B. Ric-8B promotes functional expression of odorant receptors. *Proc. Natl Acad. Sci. USA* **103**, 9310–9314 (2006).
54. Raveh, A., Cooper, A., Guy-David, L. & Reuveny, E. Nonenzymatic rapid control of GIRK channel function by a G protein-coupled receptor kinase. *Cell* **143**, 750–760 (2010).
55. Zheng, S. Q. et al. MotionCor2: anisotropic correction of beam-induced motion for improved cryo-electron microscopy. *Nat. Methods* **14**, 331–332 (2017).
56. Ferreira, F. P., Goulart, M. D., de Almeida-Pedrin, R. R., Conti, A. C. & Cardoso, M. A. Treatment of class III malocclusion: atypical extraction protocol. *Case Rep. Dent.* **2017**, 4652685 (2017).
57. Bepler, T., Kelley, K., Noble, A. J. & Berger, B. Topaz-Denoise: general deep denoising models for cryoEM and cryoET. *Nat. Commun.* **11**, 5208 (2020).
58. Emsley, P., Lohkamp, B., Scott, W. G. & Cowtan, K. Features and development of Coot. *Acta Crystallogr. D Biol. Crystallogr.* **66**, 486–501 (2010).
59. Afonine, P. V. et al. Real-space refinement in PHENIX for cryo-EM and crystallography. *Acta Crystallogr. D Struct. Biol.* **74**, 531–544 (2018).
60. Goddard, T. D. et al. UCSF ChimeraX: meeting modern challenges in visualization and analysis. *Protein Sci.* **27**, 14–25 (2018).
61. Masuho, I., Martemyanov, K. A. & Lambert, N. A. Monitoring G protein activation in cells with BRET. *Methods Mol. Biol.* **1335**, 107–113 (2015).
62. Jo, S., Kim, T., Iyer, V. G. & Im, W. CHARMM-GUI: a web-based graphical user interface for CHARMM. *J. Comput. Chem.* **29**, 1859–1865 (2008).
63. Wu, E. L. et al. CHARMM-GUI Membrane Builder toward realistic biological membrane simulations. *J. Comput. Chem.* **35**, 1997–2004 (2014).
64. Vanommeslaeghe, K. et al. CHARMM general force field: a force field for drug-like molecules compatible with the CHARMM all-atom additive biological force fields. *J. Comput. Chem.* **31**, 671–690 (2010).

Acknowledgements

We thank B. Kobilka and K. Suzuki for helpful discussion, H. Hisano and H. Ikeda for expression and purification of the ghrelin receptor–miniG$_q$ complex and N. Nomura for the supply of cells expressing Nb35 or scFv16 and for advice on purification. This work was supported by startup funding from Sanford Research (to I.M.), JSPS KAKENHI grants 18K16217 (to Y.S.), 20K06531 (to M.K. and Y.S.), 20KK0359 (to Y.S.), 22KK0099 (to H.A., Y.S. and D.I.), 24K01965 (to Y.S.) and 24K01984 (to S.Y.), the Takeda Science Foundation (to Y.S. and M.K.), the Kobayashi Foundation (Y.S.), the Naito Foundation (M.K.), and the Research Support Project for Life Science and Drug Discovery (Basis for Supporting Innovative Drug Discovery and Life Science Research) from AMED under grant numbers JP23ama121007 (to S.I), JP23ama121001 (to D.I.) and JP24ama121013 (to T.M.).

Author contributions

Y.S. designed the expression construct, optimized the purification procedure and conducted the cell surface expression assay. Y.S. and

H.A. purified the ghrelin receptor–miniG$_q$ protein complex. D.I., H.A. and J.K. carried out the cryo-EM analysis under the guidance of T.K. D.I. and H.A. determined the structure with supervision from S.I. Y.S. and K.M. performed a Ca^{2+} mobilization assay with guidance from M.K. R.T. was responsible for most BRET experiments and data analysis. R.K. investigated the intrinsic biochemical properties of ghrelin-bound ghrelin receptor. E.K. analyzed the binding mechanisms of ligands to the ghrelin receptor, as well as the structural changes associated with ligand binding. S.Y. performed the MD simulation. H.W.-M. undertook the analyses of natural genetic variations and binding mechanisms of ligands to the ghrelin receptor and maintained the cells for BRET experiments. Y.S., D.I. and I.M. wrote the paper with input from all authors. The project was overseen by T.M., M.K., S.I. and I.M. M.K. and S.I. were responsible for structural analyses. I.M. was responsible for project design, data interpretation and writing of the paper.

Competing interests

The authors declare no competing interests.

Additional information

Extended data is available for this paper at https://doi.org/10.1038/s41594-024-01481-6.

Supplementary information The online version contains supplementary material available at https://doi.org/10.1038/s41594-024-01481-6.

Correspondence and requests for materials should be addressed to Yuki Shiimura, So Iwata or Ikuo Masuho.

Peer review information *Nature Structural & Molecular Biology* thanks Osamu Nureki, Jin-Peng Sun and the other, anonymous, reviewer(s) for their contribution to the peer review of this work. Primary Handling Editor: Katarzyna Ciazynska, in collaboration with the *Nature Structural & Molecular Biology* team.

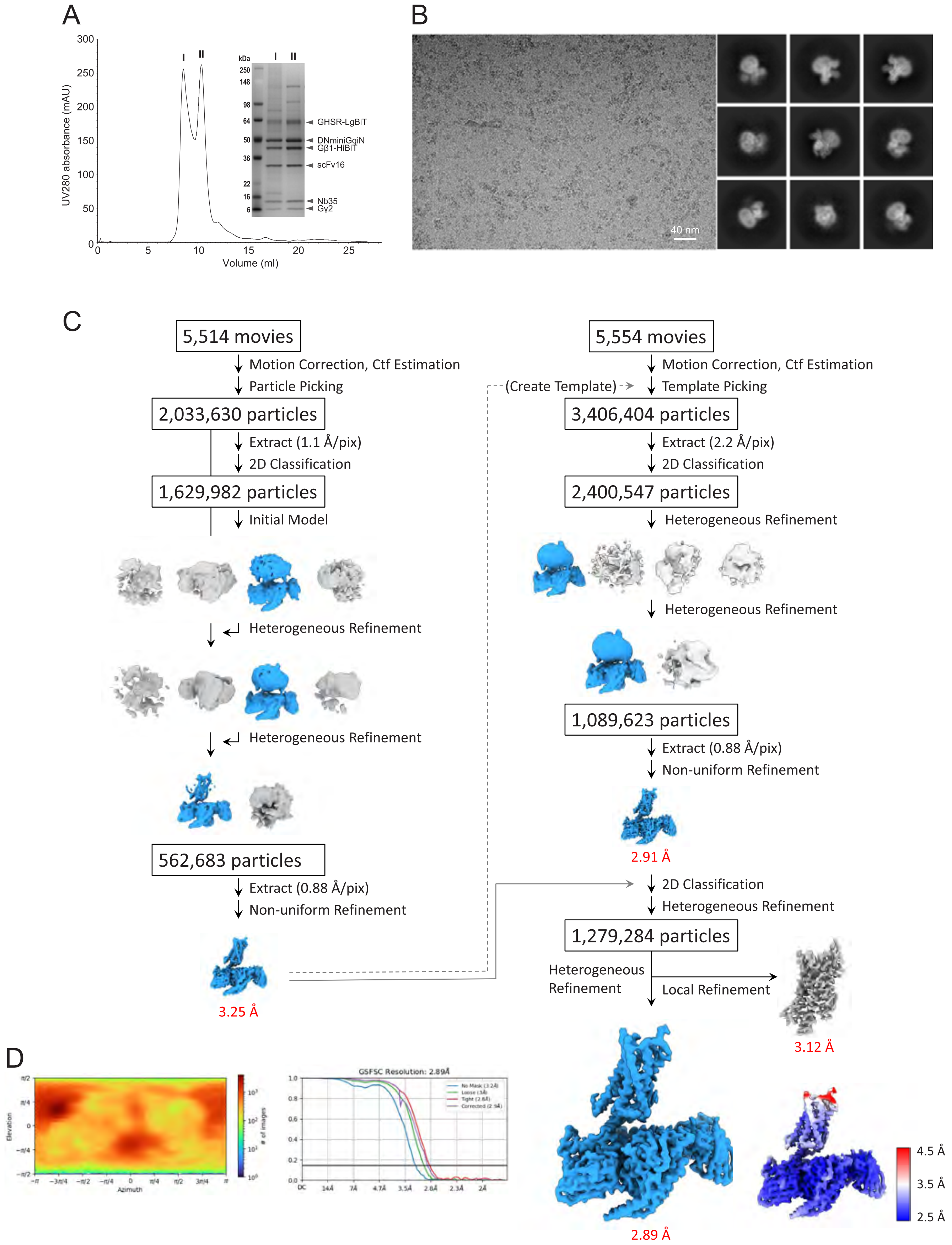

Extended Data Fig. 1 | See next page for caption.

Extended Data Fig. 1 | Single-particle cryo-EM analysis procedure. (**a**) Representative elution profile of the purified anamorelin-bound ghrelin receptor-miniG$_q$ complex from a size exclusion column, along with its Coomassie Brilliant Blue (CBB) staining. Peak I represent the void peak. Purification and CBB staining were performed more than five times, consistently yielding similar results. (**b**) Representative cryo-EM micrographs and two-dimensional classification averages of the anamorelin-bound ghrelin receptor-miniG$_q$ complex. A total of 11,068 micrographs were acquired using a Titan Krios microscope. (**c**) Cryo-EM data processing workflows of the anamorelin-bound ghrelin recepro-miniG$_q$ complex. The final cryo-EM map is colored according to local resolution (Å). (**d**) Euler angle distributions of the particles used for final reconstruction (left) and the global GSFSC curve for the final 3D density map (right).

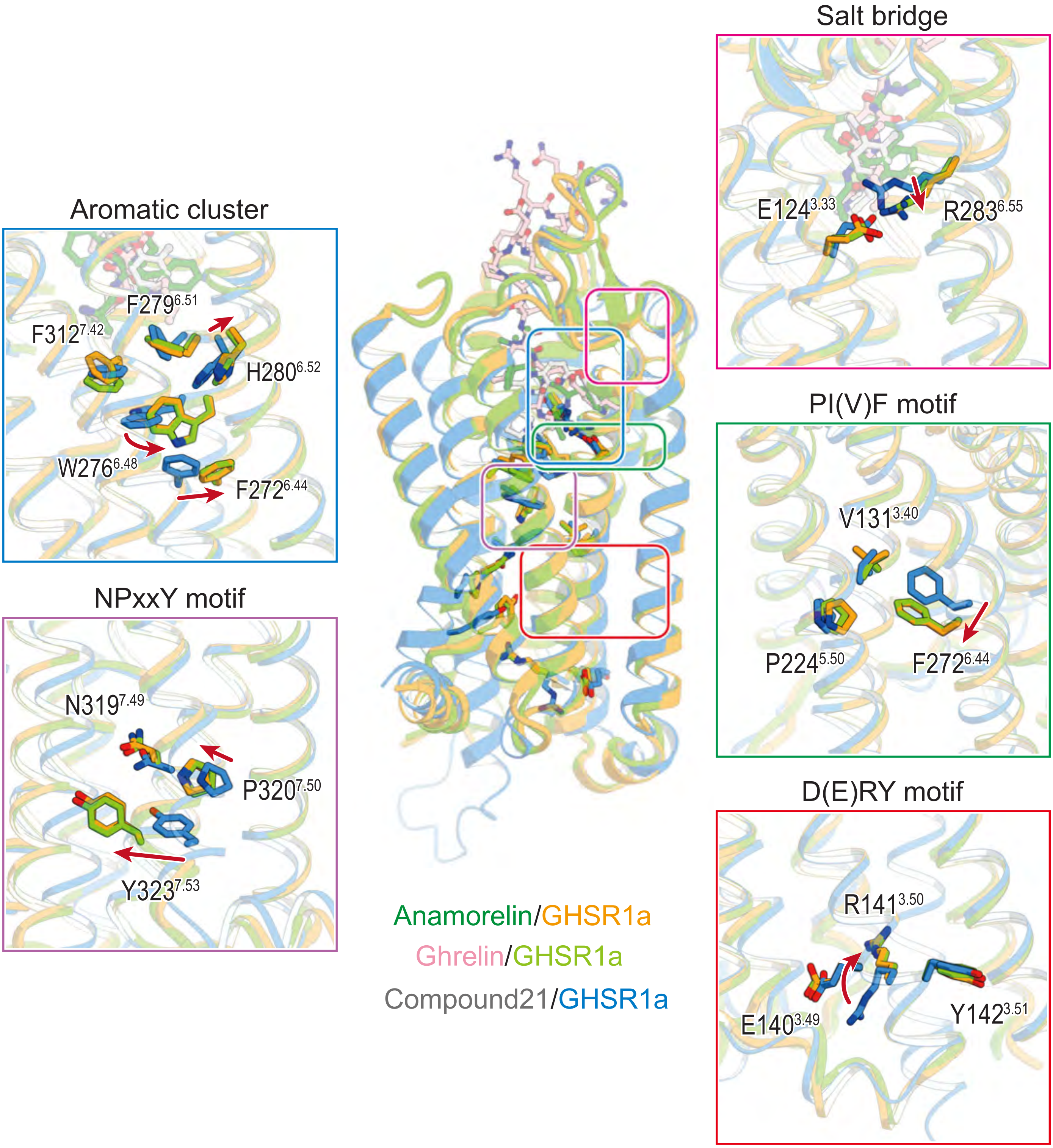

Extended Data Fig. 2 | Motif comparisons. A comparison of conserved motifs in structures bound to anamorelin (PDB ID: 8JSR), ghrelin (PDB ID: 7F9Y), and CPD21 (PDB ID: 6KO5). The locations of the motifs are indicated by colored boxes: magenta, salt bridge; blue, aromatic cluster; green, PI(V)F; purple, NPxxY; and red, D(E)RY. The movements of side chains that undergo significant changes upon activation of the ghrelin receptor are indicated with red arrows.

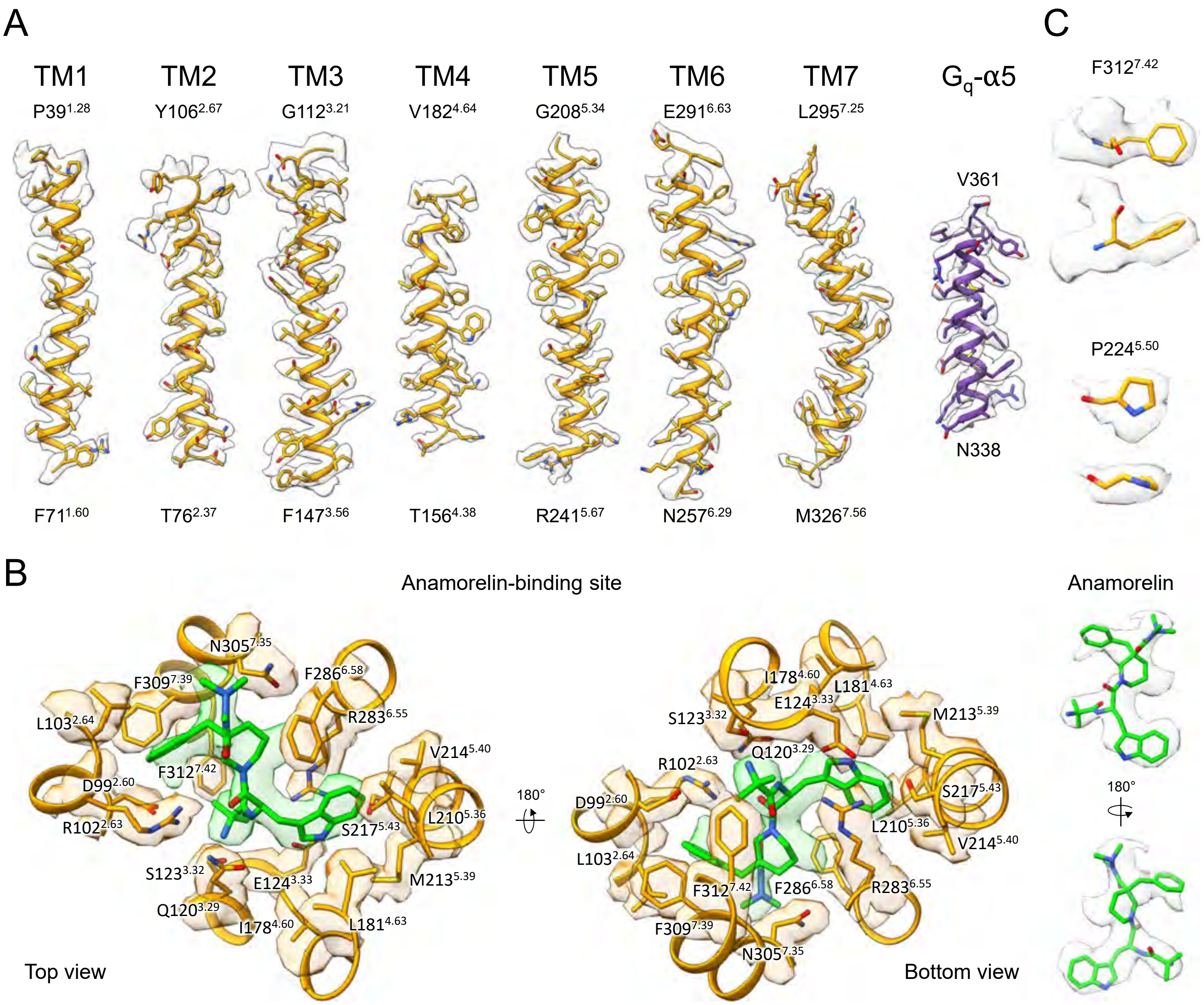

Extended Data Fig. 3 | Cryo-EM density map. (**a**) The transmembrane helices 1-7, and the α5 helix of the miniG$_q$ of the anamolerin-bound ghrelin receptor-miniG$_q$ complex. (**b**) The agonist-binding site of the anamolerin-bound ghrelin receptor-miniG$_q$ complex. (**c**) The density map of amino acid residues showing the orientation specific to the anamorelin-bound structure.

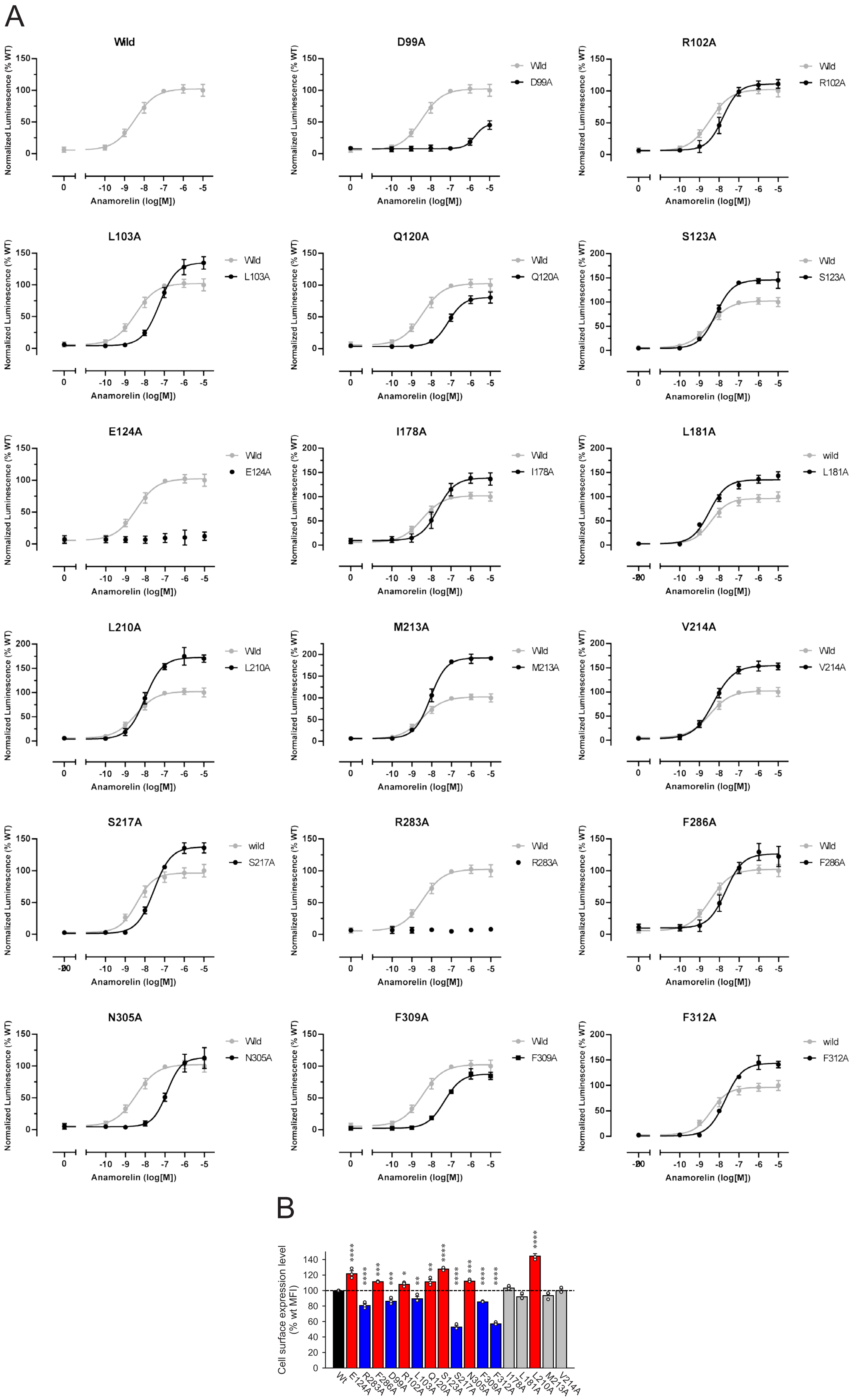

Extended Data Fig. 4 | See next page for caption.

Extended Data Fig. 4 | Dose response analysis and expression levels of functional receptors on the plasma membrane. (**a**) Ca^{2+} mobilization assay for ghrelin receptor mutants. Wild-type and alanine mutants are shown in gray and black, respectively. The change in maximum $[Ca^{2+}]i$ upon the addition of each concentration of anamorelin was determined in quadruplicate (n = 4 wells). Symbols and error bars represent mean and standard error. A representative result from three independent experiments with similar results was presented. (**b**) Cell surface expression levels of wild-type and mutant ghrelin receptors. The wild-type and mutant receptors were fluorescently labeled through an N-terminal Flag tag on each receptor. The expression levels of the mutants were quantified by calculating the ratio of green fluorescence intensity to that of the wild type. The expression levels of each mutant were 50–145% of the wild type, except for $L210^{5.36}A$, $S217^{5.43}A$, and $F312^{7.42}A$. Statistics: results are expressed as mean ± SD (One-way ANOVA followed by Dunnett multiple comparison test, $P < 0.05$, $^{**}P < 0.01$, $^{***}P < 0.001$, and $^{****}P < 0.0001$; n = 3 wells). Adjusted P values in comparison with the wild-type receptor are as follows: <0.0001 for E124E, R283A, S123A, S217A, F309A, F312A, and L210A; 0.0001 for D99A; 0.0003 for N305A; 0.0009 for F286A; 0.0012 for Q120A; 0.0041 for L103A; 0.0400 for R102A; 0.0608 for L181A; 0.2281 for M213A; 0.9076 for I178A; >0.9999 for V214A.

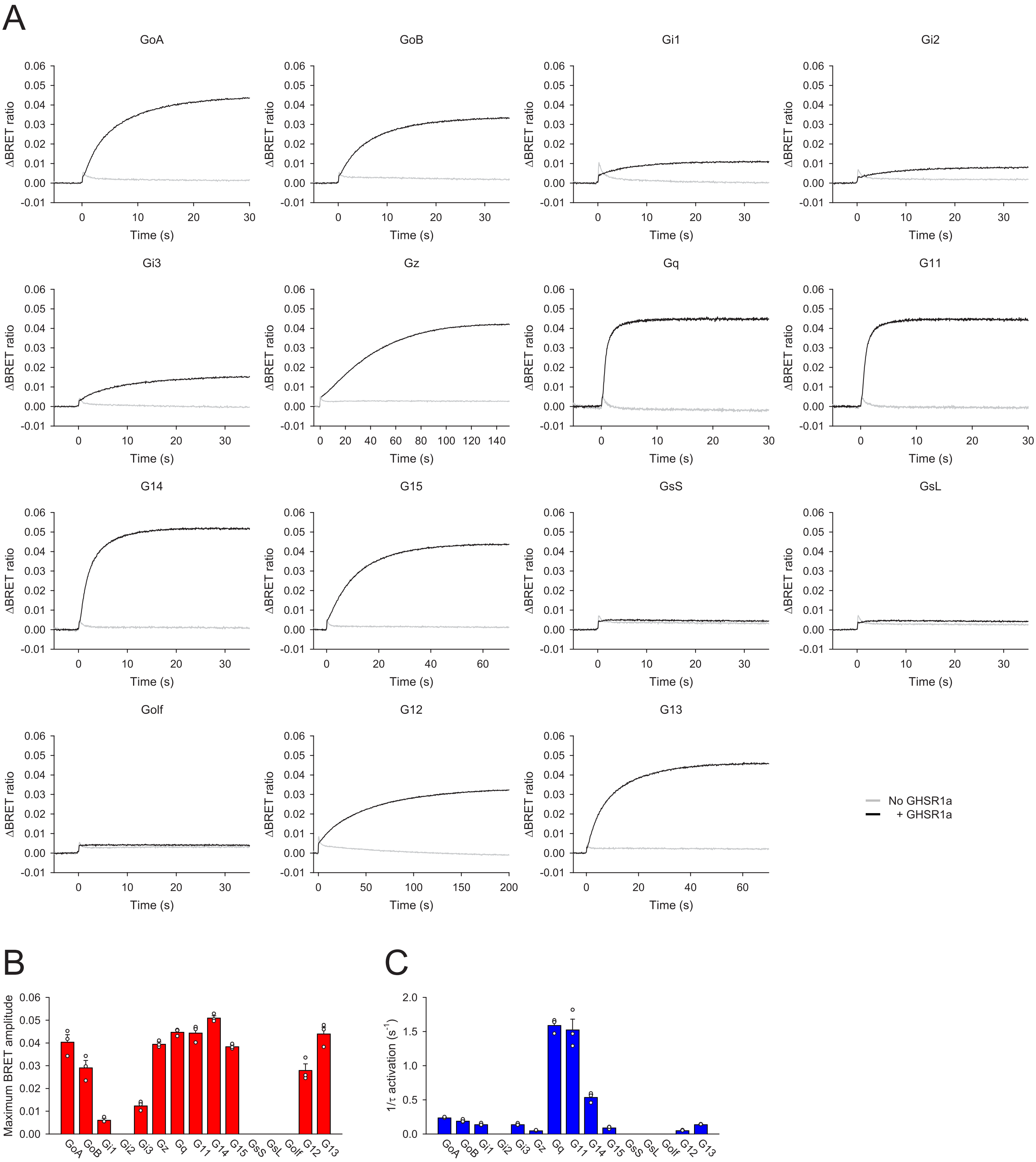

Extended Data Fig. 5 | Investigating the ghrelin-induced G protein-coupling profile of the ghrelin receptor. (**a**-**c**) Real-time monitoring of G protein activation by the ghrelin receptor. The saturated concentration of ghrelin (10 μM) was applied at time point 0, and the change in BRET signal was monitored (**a**). The maximum amplitude of the response (**b**) and activation rates (**c**) are presented as bar graphs. The traces represent the mean values of three independent experiments (**a**). Mean ± SEM of three independent experiments is shown (**b** and **c**).

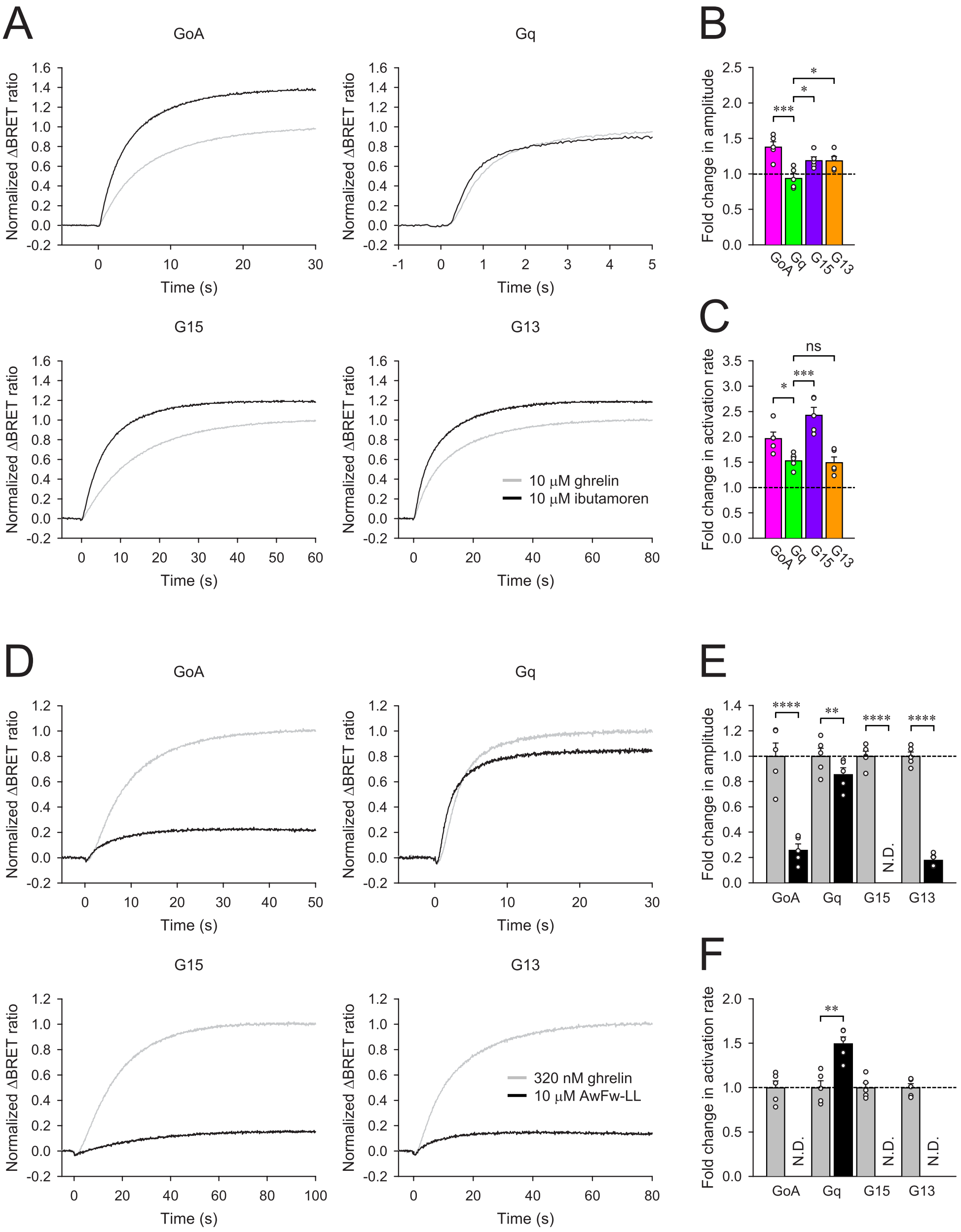

Extended Data Fig. 6 | Quantitative analysis of ibutamoren and AwFw-LL properties on the ghrelin receptor. (**a-f**) Quantitative characterization of the response induced by ibutamoren (**a-c**) and AwFw-LL (**d-f**) compared to ghrelin using the *in cellulo* GEF assay. (**a**) Normalized BRET responses to the maximum amplitude induced by ghrelin are shown. (**b** and **c**) The maximum amplitude (**b**) and activation rates (**c**) induced by ibutamoren, presented as fold change in comparison to the ghrelin-induce response, are shown as bar graphs. (**d**) Normalized BRET responses to the maximum amplitude induced by ghrelin are shown. (**e** and **f**) The maximum amplitude (**e**) and activation rates (**f**) induced by AwFw-LL, presented as fold change in comparison to the ghrelin-induced response, are shown as bar graphs. The traces represent the mean values of five independent experiments (**a** and **d**). Mean ± SEM of five independent experiments are shown (**b-c** and **e-f**). 'N.D.' indicates not detected (**e**). Statistical significance was determined by One-Way ANOVA followed by Dunnett multiple comparison test (**b** and **c**) and Two-Way ANOVA with Šídák multiple comparison test (**e** and **f**), with significance indicated by asterisks (*P < 0.05, **P < 0.01, ***P < 0.001, ****P < 0.0001). Adjusted P values are as follows: 0.0003 for Gq vs. GoA, 0.0290 for Gq vs. G15, and 0.0307 for Gq vs. G13 in panel **b**; 0.0463 for Gq vs. GoA, 0.0002 for Gq vs. G15, and 0.9907 for Gq vs. G13 in panel **c**; <0.0001 for GoA, G15, and G13, and 0.0055 for Gq in panel **e**; 0.0002 for GoA, 0.0034 for Gq, <0.0001 for G15, and 0.0009 for G13 in panel **f**. "N.D." indicates that the response was not determined (**f**) due to small responses that could not be accurately quantified for activation rates.

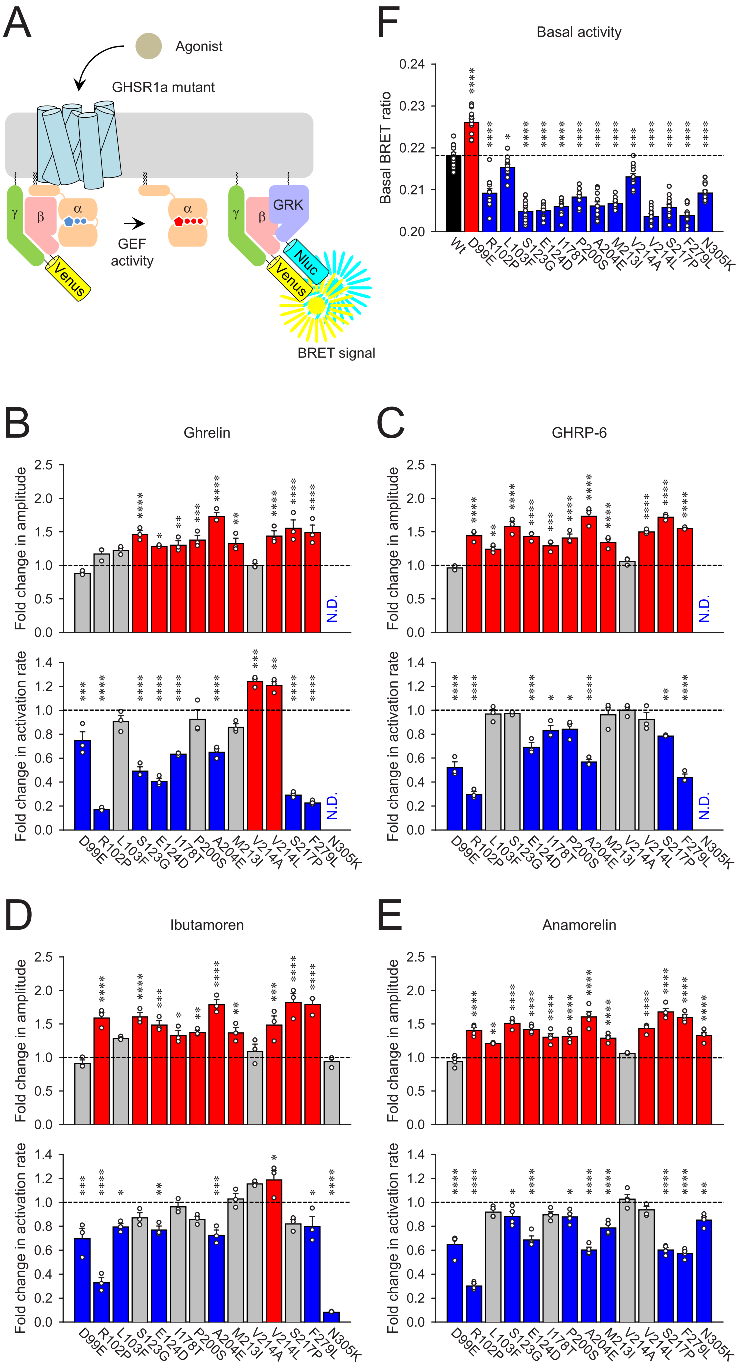

Extended Data Fig. 7 | See next page for caption.

Extended Data Fig. 7 | Impact of natural genetic variations in the orthosteric ligand-binding pocket on agonist actions. (**a**) Schematic representation of the BRET-based kinetic assay used for real-time monitoring of the ghrelin receptor's activity on G_q following agonist stimulation. (**b-e**) The response of 14 ghrelin receptor mutants to various agonists (10 µM ghrelin, 10 µM GHRP-6, 10 µM ibutamoren, and 10 µM anamorelin) was examined, focusing on the activation of G_q as a functional readout of the mutant receptors. Bar graphs represent the fold change compared to the wild-type receptor-induced response, illustrating the maximum amplitude and the speed of G protein activation induced by each agonist. The basal activity of the ghrelin receptor was also examined (**f**). Mean ± SEM of four independent experiments (**e**), three independent experiments (**b-d**), or thirteen independent experiments (**f**) are shown. Statistical significance was determined by One-Way ANOVA followed by Dunnett multiple comparison test (**b-f**), with significance indicated by asterisks (*$P < 0.05$, **$P < 0.01$, ***$P < 0.001$, ****$P < 0.0001$). Adjusted P values in comparison with the wild-type receptor are as follows: <0.0001 for S123G, A204E, V214L, S217P, F279L, and N305K, 0.0005 for P200S, 0.0028 for M213I, 0.0066 for I178T, 0.0121 for E124D, 0.0769 for L103F, 0.2792 for R102P, 0.7626 for D99E, and >0.9999 for V214A in panel **b** (amplitude); <0.0001 for D99E, R102P, S123G, E124D, I178T, A204E, S217P, F279L, and N305K, 0.0002 for V214A, 0.0014 for V214L, 0.0605 for M213I, 0.4336 for L103F, and 0.6960 for P200S in panel **b** (activation rate); <0.0001 for R102P, S123G, E124D, P200S, A204E, M213I, V214L, S217P, and F279L, 0.0004 for I178T, 0.0037 for L103F, 0.9437 for V214A, and 0.9999 for D99E in panel **c** (amplitude); <0.0001 for D99E, R102P, E124D, A204E, and F279, 0.0026 for S217P, 0.0219 for I178T, 0.0405 for P200S, 0.6703 for V214L, 0.9963 for M213I, 0.9995 for L103F, and >0.9999 for S123G and V214A in panel **c** (activation rate); <0.0001 for R102P, S123G, A204E, S217P, and F279L, 0.0003 for E124D and V214L, 0.0071 for P200S, 0.0085 for M213I, 0.0231 for I178T, 0.0667 for L103F, 0.9766 for V214A, 0.9945 for D99E, and >0.9999 for N305K in panel **d** (amplitude); <0.0001 for R102P and N305K, 0.0002 for D99E, 0.0008 for A204E, 0.0066 for E124D, 0.0197 for L103F, 0.0243 for F279L, 0.0343 for V214L, 0.0537 for S217P, 0.1246 for V214A, 0.2056 for P200S, 0.3043 for S123G, 0.9998 for I178T, and >0.9999 for M213I in panel **d** (activation rate); <0.0001 for R102P, S123G, E124D, I178T, P200S, A204E, M213I, V214L, S217P, F279L, and N305K, 0.0055 for L103F, 0.9053 for V214A, and 0.9773 for D99E in panel **e** (amplitude); <0.0001 for D99E, R102P, E124D, A204E, M213I, S217P, and F279L, 0.0046 for N305K, 0.0312 for P200S, 0.0427 for S123G, 0.0948 for I178T, 0.3042 for L103F, 0.6292 for V214L, and 0.9963 for V214A in panel **e** (activation rate); and <0.0001 for D99E, R102P, S123G, E124D, I178T, P200S, A204E, M213I, V214L, S217P, F279L, and N305K, 0.0007 for V214A, and 0.10172 for L103F in panel **f**. 'N.D.' indicates not detected.

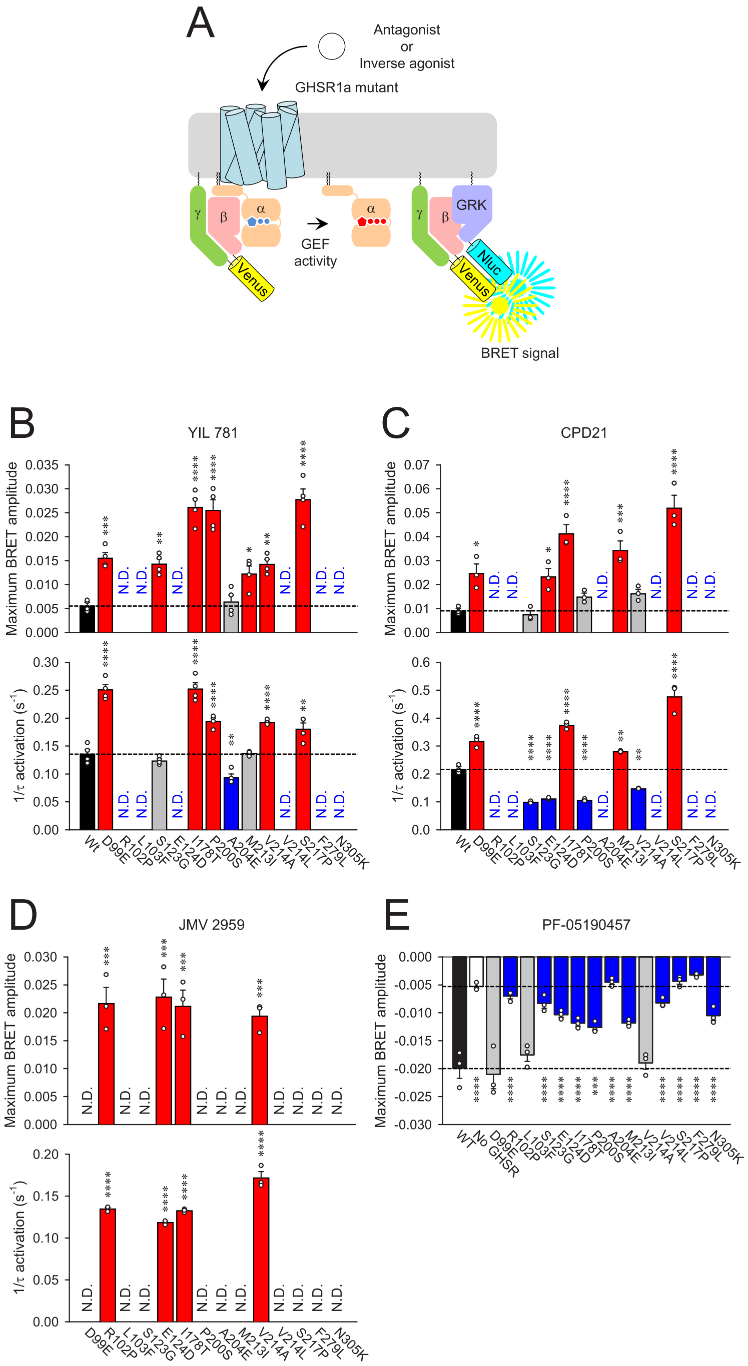

Extended Data Fig. 8 | Impact of natural genetic variations in the orthosteric ligand-binding pocket on antagonist/inverse agonist actions. (**a**) Schematic representation of the BRET-based kinetic assay used for real-time monitoring of the ghrelin receptor's activity on G_q following antagonist/inverse agonist stimulation. (**b-e**) The response of 14 ghrelin receptor mutants to various ligands (100 µM YIL 781, 32 µM CPD21, 100 µM JMV 2959, and 10 µM PF-05190457) was examined, focusing on the activation of G_q as a functional readout of the mutant receptors. Bar graphs illustrate the maximum amplitude and the speed of G protein activation induced by each ligand. G_q deactivation induced by an inverse agonist was quantified (**e**). Mean ± SEM of four independent experiments (**b**) or three independent experiments (**c-e**) are shown. Statistical significance was determined by One-Way ANOVA with Dunnett multiple comparison test (**b, c, d,** and **e**), with significance indicated by asterisks (*$P < 0.05$, **$P < 0.01$, ***$P < 0.001$, ****$P < 0.0001$). Adjusted P values in comparison with the wild-type receptor are as follows: <0.0001 for I178T, P200S, and S217P, 0.0005 for D99E, 0.0023 for S123G, 0.0024 for V214A, 0.0245 for M213I, and 0.9996 for A204E in panel **b** (amplitude); <0.0001 for D99E, I178T, P200S, and V214A, 0.0011 for S217P, 0.0020 for A204E, 0.7644 for S123G, and >0.9999 for M213I in panel **b** (activation rate); <0.0001 for I178T and S217P, 0.0002 for M213I, 0.0173 for D99E, 0.0330 for E124D, 0.5048 for V214A, 0.7065 for P200S, and 0.9998 for S123G in panel **c** (amplitude); <0.0001 for D99E, S123G, E124D, I178T, P200S, and S217P, 0.0038 for V214A, and 0.0080 for M213I in panel **c** (activation rate); 0.0002 for E124D, 0.0003 for R102P and I178T, and 0.0007 for V214A in panel **d** (amplitude); <0.0001 for R102P, E124D, I178T, and V214A in panel **d** (activation rate); <0.0001 for no GHSR, S213G, E124D, I178T, A204E, M213I, V214L, S217P, F279L, and N305K, 0.0002 for P200S, 0.6001 for L103F, 0.9942 for D99E, and 0.9994 for V214A in panel **e**. 'N.D.' indicates not detected.

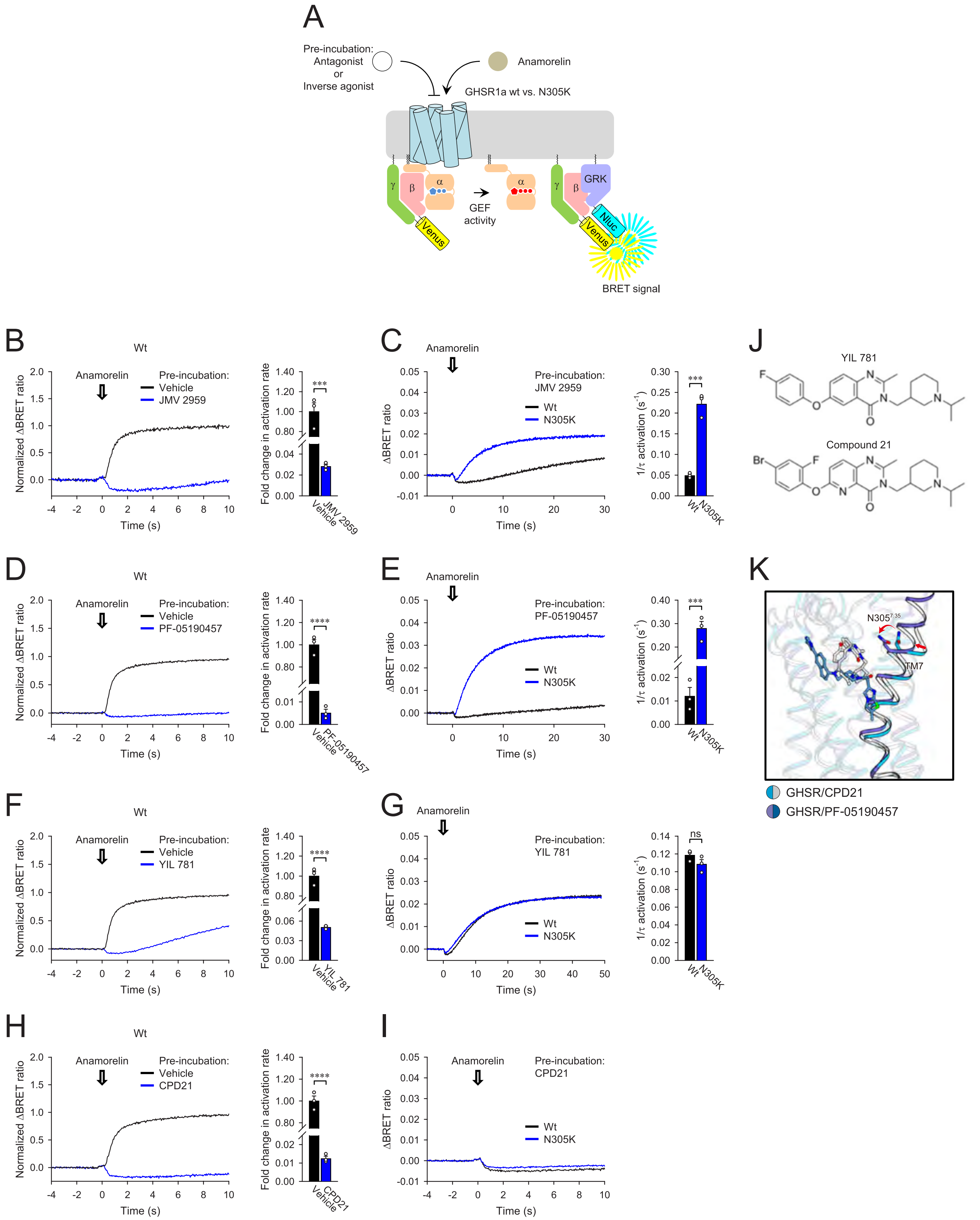

Extended Data Fig. 9 | Impact of N305$^{7.35}$K mutations on drug actions. (**a**) Assay design to examine the antagonist/inverse agonist action of the N305$^{7.35}$K mutant compared to the wild-type ghrelin receptor. (**b-i**) Effects of JMV 2959, PF-05190457, YIL 781, or CDP21 on wild-type ghrelin receptor (**b, d, f,** and **h**) and N305$^{7.35}$K mutant (**c, e, g,** and **i**). Transfected cells were pre-incubated with 100 μM JMV 2959, 10 μM PF-05190457, 10 μM YIL 781, or 32 μM CPD21 for 1 min and then stimulated with 10 μM anamorelin. The traces represent the mean values of three independent experiments. Mean ± SEM are presented as bar graphs. Statistical significance was determined by unpaired two-tailed t test, with significance indicated by asterisks (*$P < 0.05$, **$P < 0.01$, ***$P < 0.001$, ****$P < 0.0001$). Adjusted P values are as follows: 0.0004 (**b**), 0.0005 (**c**), <0.0001 (**d**), 0.0009 (**e**), <0.0001 (**f**), 0.1809 (**g**), and <0.0001 (**h**). (**j**) Comparison of the chemical structures of YIL 781 and CPD21. (**k**) Binding modes of N305$^{7.35}$ and CPD21 or PF-05190457.

nature portfolio

Corresponding author(s): Yuki Shiimura, So Iwata, Ikuo Masuho

Last updated by author(s): Dec 12, 2024

Reporting Summary

Nature Portfolio wishes to improve the reproducibility of the work that we publish. This form provides structure for consistency and transparency in reporting. For further information on Nature Portfolio policies, see our Editorial Policies and the Editorial Policy Checklist.

Statistics

For all statistical analyses, confirm that the following items are present in the figure legend, table legend, main text, or Methods section.

n/a	Confirmed	
☐	☒	The exact sample size (*n*) for each experimental group/condition, given as a discrete number and unit of measurement
☐	☒	A statement on whether measurements were taken from distinct samples or whether the same sample was measured repeatedly
☐	☒	The statistical test(s) used AND whether they are one- or two-sided *Only common tests should be described solely by name; describe more complex techniques in the Methods section.*
☒	☐	A description of all covariates tested
☐	☒	A description of any assumptions or corrections, such as tests of normality and adjustment for multiple comparisons
☐	☒	A full description of the statistical parameters including central tendency (e.g. means) or other basic estimates (e.g. regression coefficient) AND variation (e.g. standard deviation) or associated estimates of uncertainty (e.g. confidence intervals)
☐	☒	For null hypothesis testing, the test statistic (e.g. *F*, *t*, *r*) with confidence intervals, effect sizes, degrees of freedom and *P* value noted *Give P values as exact values whenever suitable.*
☒	☐	For Bayesian analysis, information on the choice of priors and Markov chain Monte Carlo settings
☒	☐	For hierarchical and complex designs, identification of the appropriate level for tests and full reporting of outcomes
☒	☐	Estimates of effect sizes (e.g. Cohen's *d*, Pearson's *r*), indicating how they were calculated

Our web collection on statistics for biologists contains articles on many of the points above.

Software and code

Policy information about availability of computer code

Data collection	Automated data collection was performed on the Titan Krios at 300 kV accelerating voltage in the Institute for Protein Research, Osaka University (Osaka, Japan).
Data analysis	Cryo-EM micrographs were recorded using a Gatan K3 detector in counting mode with a pixel size 0.88 Å using the SerialEM software (3.8). Structures were solved and refined using the Phenix software suite (1.18.X - 1.20.X) and Coot (0.8.0 and 0.9.5). Signaling assays were analyzed using Graphpad Prism 9 and SigmaPlot 14.5. CryoSPARC (3.2.0 - 4.1.1), CueMol (2.2.3), Cytosoft (5.3.1) and UCSF ChimeraX (1.7.1) were also used in this study.

For manuscripts utilizing custom algorithms or software that are central to the research but not yet described in published literature, software must be made available to editors and reviewers. We strongly encourage code deposition in a community repository (e.g. GitHub). See the Nature Portfolio guidelines for submitting code & software for further information.

Data

Policy information about availability of data

All manuscripts must include a data availability statement. This statement should provide the following information, where applicable:

- Accession codes, unique identifiers, or web links for publicly available datasets
- A description of any restrictions on data availability
- For clinical datasets or third party data, please ensure that the statement adheres to our policy

The cryo-EM density maps and atomic coordinates have been deposited in the Electron Microscopy Data Bank (EMDB) and wwPDB under accession numbers EMD-36627 and 8JSR for the anamorelin bound-ghrelin receptor-Gq complex. Source data are provided with this paper. The data that support this study are available from the corresponding authors upon request.

Research involving human participants, their data, or biological material

Policy information about studies with human participants or human data. See also policy information about sex, gender (identity/presentation), and sexual orientation and race, ethnicity and racism.

Reporting on sex and gender	N/A
Reporting on race, ethnicity, or other socially relevant groupings	N/A
Population characteristics	N/A
Recruitment	N/A
Ethics oversight	N/A

Note that full information on the approval of the study protocol must also be provided in the manuscript.

Field-specific reporting

Please select the one below that is the best fit for your research. If you are not sure, read the appropriate sections before making your selection.

☒ Life sciences ☐ Behavioural & social sciences ☐ Ecological, evolutionary & environmental sciences

For a reference copy of the document with all sections, see nature.com/documents/nr-reporting-summary-flat.pdf

Life sciences study design

All studies must disclose on these points even when the disclosure is negative.

Sample size	Sample sizes were not predetermined using formal statistical methods. For cryo-EM data, sample sizes were dictated by the availability of the microscope, with image collection continuing until resolution and 3D reconstruction converged, ensuring high-quality structural analysis. For functional assays, a minimum of three independent experiments was conducted. This sample size was chosen as it balances experimental feasibility with statistical reliability, achieving significance ($p < 0.05$) under assumptions of moderate effect sizes, as commonly observed in similar studies.
Data exclusions	Data with evident issues encountered during the experimental process were excluded from the analysis to ensure accuracy and reliability.
Replication	Protein samples were purified from separate batches and used for the cryo-EM study. Initial quality assessment involved at least three data collection sessions on a screening cryo-EM machine (Glacios, 200 kV) to confirm sample quality. Subsequently, an additional purification batch was prepared, and two data collection sessions were performed on a high-end cryo-EM machine (Titan Krios, 300 kV). Analysis of these datasets confirmed that the results were consistent across all batches. Furthermore, cell biological experiments were independently repeated three or more times, yielding reproducible findings and ensuring the reliability of the results.
Randomization	Randomization was not applicable to this study, as data collection was automated and did not involve any selection processes.
Blinding	Blinding is not applicable to structural determination studies. For cryo-EM, imaging data were collected automatically using predefined parameters, eliminating subjective bias during data acquisition. For functional analysis, blinding was deemed unnecessary due to the inherently quantitative nature of the experiments. Measurements were performed using objective and automated readouts, such as luminescence or fluorescence intensities, which are not influenced by operator interpretation. Additionally, experimental conditions were standardized across replicates, ensuring consistency and minimizing the risk of bias.

Reporting for specific materials, systems and methods

We require information from authors about some types of materials, experimental systems and methods used in many studies. Here, indicate whether each material, system or method listed is relevant to your study. If you are not sure if a list item applies to your research, read the appropriate section before selecting a response.

Materials & experimental systems

n/a	Involved in the study
☐	☒ Antibodies
☐	☒ Eukaryotic cell lines
☒	☐ Palaeontology and archaeology
☒	☐ Animals and other organisms
☒	☐ Clinical data
☒	☐ Dual use research of concern
☒	☐ Plants

Methods

n/a	Involved in the study
☒	☐ ChIP-seq
☐	☒ Flow cytometry
☒	☐ MRI-based neuroimaging

Antibodies

Antibodies used	Anti-DYKDDDDK tag monoclonal antibody, clone No.1E6 Supplier: Fujifilm Wako Catalog number: 014-22383 Dilution: 2.5 µg per ml Goat anti-mouse IgG (H+L) antibody, Alexa Fluor 488 Supplier: Thermo Fisher Catalog number: A-11001 Dilution: 5 µg per ml
Validation	The antibody used in this study was commercially purchased and validated by the vendor. Detailed validation data can be accessed on the vendor's website.

Eukaryotic cell lines

Policy information about cell lines and Sex and Gender in Research

Cell line source(s)	Sf9 (Cat. No. B82501) were purchased from Thermo Fisher Scientific. CHO-K1 (Cat. No. CCL-61), HEK293 (CRL-1573), and HEK293T/17 (Cat. No. CRL-11268) cells were obtained from ATCC.
Authentication	None of the cell lines were independently authenticated, as they were sourced from reputable suppliers (Thermo Fisher Scientific and ATCC) that provide verified cell lines.
Mycoplasma contamination	All cell lines were tested for mycoplasma contamination and confirmed to be free of contamination before use.
Commonly misidentified lines (See ICLAC register)	None of the cell lines used in this study are listed among commonly misidentified cell lines according to the ICLAC database.

Plants

Seed stocks	N/A
Novel plant genotypes	N/A
Authentication	N/A

Flow Cytometry

Plots

Confirm that:

☐ The axis labels state the marker and fluorochrome used (e.g. CD4-FITC).

☐ The axis scales are clearly visible. Include numbers along axes only for bottom left plot of group (a 'group' is an analysis of identical markers).

☐ All plots are contour plots with outliers or pseudocolor plots.

☒ A numerical value for number of cells or percentage (with statistics) is provided.

Methodology

Sample preparation	Sample preparation were explained in The Methods.
Instrument	Guava EasyCyte Plus (Millipore)
Software	CytoSoft 5.3.1
Cell population abundance	Approximately 10,000 cellular events were collected and the total fluorescence intensity of positive expression cell population was calculated.
Gating strategy	Gating was determined by the Alexa Fluor™ 488 fluorescence intensity to differentiate positive cells and all other cells.

☐ Tick this box to confirm that a figure exemplifying the gating strategy is provided in the Supplementary Information.